



# Optimization of Pd catalysts supported on $\text{Co}_3\text{O}_4$ for low-temperature lean combustion of residual methane

Giuliana Ercolino<sup>a</sup>, Paweł Stelmachowski<sup>a,b,\*</sup>, Gabriela Grzybek<sup>b</sup>, Andrzej Kotarba<sup>b</sup>, Stefania Specchia<sup>a,\*</sup>

<sup>a</sup> Department of Applied Science and Technology, Politecnico di Torino, Corso Duca degli Abruzzi 24, 10129 Torino, Italy

<sup>b</sup> Faculty of Chemistry, Jagiellonian University in Kraków, ul. Ingardena 3, 30-060 Kraków, Poland

## ARTICLE INFO

### Article history:

Received 5 November 2016

Received in revised form 16 January 2017

Accepted 22 January 2017

Available online 23 January 2017

### Keywords:

Palladium

Cobalt spinel

Urea

Methane combustion

Lean conditions

## ABSTRACT

A series of Pd/ $\text{Co}_3\text{O}_4$  catalysts with increasing palladium loading in the range of 0.5–5 wt.% was prepared by incipient wetness impregnation of  $\text{Co}_3\text{O}_4$ . Solution combustion synthesis with urea as a fuel was used to optimize the  $\text{Co}_3\text{O}_4$  reactive support for palladium in the combustion of methane in lean conditions. The obtained catalysts were thoroughly examined by XRD, XPS, XRF, RS, FESEM, H<sub>2</sub>-TPR, TGA, and N<sub>2</sub>-BET techniques. The catalytic tests of CH<sub>4</sub> combustion were performed for 0.5, 1, and 2 vol.% CH<sub>4</sub>, with constant lambda value. The obtained results revealed that a sub-stoichiometric fuel-to-oxidizer ratio, 0.75, results in the most catalytically active  $\text{Co}_3\text{O}_4$  phase. The important differences in the catalysts' activity were apparent for the highest CH<sub>4</sub> concentration, with the 3% Pd/ $\text{Co}_3\text{O}_4$  being the most active catalyst. The observed activity was explained considering the physicochemical, spectroscopic, and microscopic characterization of the catalysts with the PdO nanocrystals surface distribution being the determining factor for the catalysts' reactivity. A simple model accounting for the observed dispersion effect is proposed. The model is based on a two types of the interaction of the surface PdO active phase with the  $\text{Co}_3\text{O}_4$  support. Firstly, cobalt oxide helps to remove hydroxyl species from the PdO surface, thus making the active sites more available for methane activation. Secondly, cobalt spinel provides lattice oxygen to the PdO phase, again helping to recreate active sites thereon.

© 2017 Elsevier B.V. All rights reserved.

## 1. Introduction

Natural gas (NG) provides an attractive alternative to gasoline as an economical fuel because it is much more abundant as a natural resource and it will be readily available for decades. The use of NG as a fuel also has environmental and economic benefits because its ignition temperature for combustion is lower than that of gasoline, and the high H/C ratio in the CH<sub>4</sub> molecule leads to the formation of more water than CO<sub>2</sub>. Moreover, NG contains very low levels of sulfur and nitrogen impurities resulting in reduced NO<sub>x</sub> and SO<sub>x</sub> emissions. On the other hand, methane is a more powerful greenhouse gas than CO<sub>2</sub>, which is why unburnt NG is an environmental problem [1]. Residual methane, or methane slip, is emitted from different human activities such as agriculture, oil and natural gas systems, coal mining, stationary and mobile combustion, biomass combustion, and vehicles fed with compressed NG (CNG) [2]. The

optimal way to abate this environmental pollutant, emitted in low concentrations (ranging for example from 0.1 to 1.5% in coal mining [3], and from 400 to 1500 ppmv for CNG vehicles [4]), is its total oxidation to water and carbon dioxide. The challenge of methane activation is related to the high stability of this compound. The non-catalytic activation of the methane C–H bond in the gas phase usually requires very a high temperature and leads mostly to radical reactions with low intrinsic selectivity [5,6]. In spite of the high stability of methane, the catalytic combustion represents a promising option to oxidize nearly 100% of the methane in the exhaust stream at a temperature above 400 °C [4,7–9], with  $T_{50}$  (temperature of 50% conversion) ranging from 410 to 460 °C, depending on the loading of noble metals [7].

Specifically, the very recent standards for CNG vehicles (the EURO VI and the US Environmental Protection Agency (EPA) greenhouse gas legislation) require very strict methane emission limits, not exceeding 0.5 g kWh<sup>-1</sup> [7], or 0.10 g km<sup>-1</sup> for passenger cars and 0.16 g km<sup>-1</sup> for light commercial vehicles [10]. These methane emission limits entail very active oxidation catalysts, containing up to 4 times higher noble metal content compared to catalytic systems for gasoline vehicles [11].

\* Corresponding author.

E-mail addresses: [pawel.stelmachowski@polito.it](mailto:pawel.stelmachowski@polito.it) (P. Stelmachowski), [stefania.specchia@polito.it](mailto:stefania.specchia@polito.it) (S. Specchia).

A proper design of the catalyst may provide a stable activity for prolonged periods of time [12–14]. Deactivation, in fact, mainly occurs because of the high temperature of the reaction and it is intensified mainly by the presence of water and S-compounds in the exhaust gasses [9,15]. Palladium-based catalysts are well known among the most active catalysts for oxidation of the organic molecules, including natural gas components [16,17]. Commercial three-way catalyst (TWC) are mainly based on bimetallic Pd–Rh [7], Pd–Pt over a mixture of La or Ba over CeO<sub>2</sub>–ZrO<sub>2</sub> [18], or Pd–Au dispersed on Al<sub>2</sub>O<sub>3</sub> [8], washcoated over ceramic or metallic structured supports (mainly monoliths or foams) with high total noble metal loadings largely exceeding 10 g L<sup>−1</sup> [7,9,18,19]. The most recent patents on commercial TWC catalysts are based on binary or ternary mixtures of non-precious metals comprised between Zr<sub>0.5</sub>Sn<sub>0.25</sub>Ti<sub>0.25</sub>O<sub>2</sub> and Sn<sub>1-x</sub>Ti<sub>x</sub>O<sub>2</sub> or CuCe(La)O<sub>2</sub> and CuZr(Y)O<sub>2</sub> [20,21], active in the range 300–550 °C.

Due to the high cost of the palladium, various alternative supported systems have been studied since many years, mostly alumina based, but also ceria or ceria-zirconia systems were reported to have a beneficial effect on the Pd-species catalytic activity [15,22–28]. Table 1 provides a rough comparison of the types and relative activity of the most recent catalytic systems for the lean combustion of methane slip [28–41]. Analysis of Table 1 shows that all of the listed catalysts, tested at powder level in plug flow quartz reactors in different amounts and reaction conditions, are behaving in similar way, with the *T*<sub>50</sub> ranging between 240 and 510 °C. Interestingly, the amount of Pd over the carriers ranges from 0.05 to 10 wt.%, and the specific surface area (SSA) of the catalysts ranges from 6 to 212 m<sup>2</sup> g<sup>−1</sup>, with the best activity belonging to the catalyst with the highest Pd content (and a relatively low SSA, 20 m<sup>2</sup> g<sup>−1</sup>).

Spinel-type Co<sub>3</sub>O<sub>4</sub> and Co<sub>3</sub>O<sub>4</sub>-based composite oxides constitute an interesting class of materials for noble metals support in the oxidation of hydrocarbons because they exhibit some intrinsic catalytic activity in this reaction. Furthermore, doping the cobalt spinel with other elements may induce phenomena which improve catalytic activity, such as structural defects (e.g. oxygen vacancies) leading to improved oxygen mobility [42], or work function lowering due to alkali surface promotion [43].

The Solution Combustion Synthesis (SCS) is a simple and economic method to synthesize an oxide powder. Moreover, compared with other methods, SCS allows effective low-cost production of stable nanomaterials at low-medium temperatures (200–600 °C), with fast heating rates and short reaction times. These characteristics lead to certain practical advantages, such as using a relatively simple equipment, cheap reactants (e.g. nitrates), and an exothermic, fast and self-sustaining reaction [14,44,45]. Various authors used in the past this technique to synthesize active catalysts for methane oxidation [39,46,47]. Recently we found that Pd/Co<sub>3</sub>O<sub>4</sub> catalysts for methane combustion were more active if prepared by SCS than by precipitation method [36]. Moreover, this synthesis method was chosen in particular for its ease of application for the possible preparation of supported catalysts on ceramic foams and monoliths, as previously reported by Vita et al. [48,49].

In the SCS, nitrates are most often used as metal precursors because NO<sub>3</sub><sup>−</sup> groups act as oxidizing agents and their high solubility in water allows for a sufficiently high solution concentration. The role of organic fuel addition is to ensure good solution homogeneity and prevent the preferential precipitation of ionic species in the first stages of the reaction and then, during the combustion process to react with the precursors. The mixture of nitrates and fuel can be ignited at relatively low temperatures, around 250 °C [35,45].

A large number of studies have focused on catalytic methane combustion over Pd-containing catalysts. Mostly metallic Pd, PdO and supported PdO have been investigated [35,50]. An important insight into the reaction mechanism has been achieved by using

quantum-chemical modeling and microkinetic analysis [51]. However, for Pd/Co<sub>3</sub>O<sub>4</sub> catalysts, which show very good activity towards oxidation reactions [52], the mechanism of CH<sub>4</sub> may be different than those on unsupported PdO. The aim of this study was to optimize Pd/Co<sub>3</sub>O<sub>4</sub> catalyst formulation, and to understand important catalysts' features determining their reactivity in a technologically relevant methane concentration range.

## 2. Materials and methods

### 2.1. Chemicals

Cobalt(II) nitrate hexahydrate, Co(NO<sub>3</sub>)<sub>2</sub>·6H<sub>2</sub>O (≥98% purity); palladium(II) nitrate hydrate, Pd(NO<sub>3</sub>)<sub>2</sub>·xH<sub>2</sub>O (≥99% purity), and urea, CH<sub>4</sub>N<sub>2</sub>O (≥99% purity) were purchased from Sigma–Aldrich. Aqueous solutions were prepared using ultrapure water obtained from a Millipore Milli-Q system with a resistivity ≈ 18 MΩ cm. For reactivity tests, pure methane, oxygen, and nitrogen gasses (purity 99.999%) were supplied in cylinders provided by SIAD company and used as received.

### 2.2. Catalysts preparation

Undoped cobalt spinels were synthesized by SCS using urea as an organic fuel and cobalt nitrate as a precursor and oxidizer. The obtained solutions were placed in an electric oven at 250 °C for 20–40 min. All samples were then calcined at 600 °C for 4 h in static air. A series of cobalt spinel supports was prepared by varying the amount of organic fuel with respect to the stoichiometric amount ( $\phi$ ) from 1.25 to 0.25. In the second part of the work, the best-performing Co<sub>3</sub>O<sub>4</sub> catalytically active support was impregnated with various amounts of palladium.

Pd-doped catalysts were prepared by depositing Pd on each of the Co<sub>3</sub>O<sub>4</sub> samples by the incipient wetness impregnation (IWI) with palladium nitrate solution, at the level from 0.5 to 5 wt.% Pd. The final calcination was done in static air for 4 h at 600 °C.

### 2.3. Physicochemical characterization

X-ray diffraction (XRD) patterns were collected using a Philips X-Pert MPD X-ray diffractometer equipped with a Cu K $\alpha$  radiation at 40 kV and 30 mA, to verify the effective composition of the catalysts and derive a qualitative indication of the presence of comparatively large noble metals crystallites from its eventually visible peaks. All powder catalysts were scanned over the 2 $\theta$  range 20°–70° over 1 h. The Co<sub>3</sub>O<sub>4</sub> diffraction peaks were assigned according to the PCPDFWIN database, ref. code 01-080-1533 (Fd3m space group). The crystal size,  $D_{XRD}$ , calculation was performed with the use of Scherrer equation and averaged for the 20 31.220° (220), 36.786° (311), 38.5° (222), 44.7° (400), 55.6° (422), 59.2° (511) and 65.1° (440) diffraction peaks.

Raman spectra were recorded at room temperature for the spectral range 100–1000 cm<sup>−1</sup>, using Renishaw InVia spectrometer and confocal microscope Leica DMLM, magnification 50 $\times$ , with CCD detector and an excitation wavelength  $\lambda$  = 514 nm. The signal-to-noise ratio was optimized by accumulating ten scans for each measurement. The minimal spot diameter of the laser on the sample for the used spectrometer is 836 nm (1.22  $\lambda$ /NA, where numerical aperture NA = 0.75 for Leica 50 $\times$  lens [53]). The applied laser power was 0.25 mW (0.5% of the 50 mW maximum laser output power).

Nitrogen physisorption was performed at −196 °C on a Micromeritics ASAP 2020 instrument. Before the measurement, about 100 mg of each sample was outgassed overnight at 150 °C in low vacuum (7 Pa). The specific surface areas (SSA) were evaluated by the BET method between 0.05 and 0.30  $p/p^0$ . Crystal sizes

**Table 1**

Recent literature review of methane combustion in lean conditions (in different operating conditions) at a glance, listed from the best to the worse catalytic activity in terms of  $T_{50}$ .

Catalyst	Available reaction conditions	$T_{50}$ °C (activity window)	Reference year
• Type and Pd content (wt.%)	• Reactive mix (vol.%)		
• SSA ( $\text{m}^2 \text{ g}^{-1}$ )	• Flow rate ( $\text{NL min}^{-1}$ )		
	• GHSV ( $\text{h}^{-1}$ ) or WHSV ( $\text{NL h}^{-1} \text{ g}^{-1}$ )		
10% Pd/ $\text{Co}_3\text{O}_4$ $20 \text{ m}^2 \text{ g}^{-1}$	1.2% $\text{CH}_4$ , 12% $\text{O}_2$ , $\text{N}_2$ balance 0.033 $\text{NL min}^{-1}$	240 (170–280)	[29] 2006
5% Pd/MWCNT (multi-walled carbon nanotubes)	0.4% $\text{CH}_4$ in air 40,000 $\text{h}^{-1}$	270 (230–330)	[30] 2016
5% Pd/ $\text{Ni-Al}_2\text{O}_3$ (7% Ni) $129 \text{ m}^2 \text{ g}^{-1}$	1% $\text{CH}_4$ in air 31 $\text{NL g}^{-1} \text{ h}^{-1}$	320 (230–460)	[31] 2013
1% Pd/ $\text{Al}_2\text{O}_3$ -NiOx (5% Ni) $32 \text{ m}^2 \text{ g}^{-1}$	0.4% $\text{CH}_4$ in air 80,000 $\text{h}^{-1}$	340 (300–500)	[32] 2013
1% Pt-Pd/ $\text{MnLaAl}_{11}\text{O}_{19}$ (0.33% Pt, 0.67% Pd) $44 \text{ m}^2 \text{ g}^{-1}$	5% $\text{CH}_4$ , 10% $\text{O}_2$ , $\text{N}_2$ balance 10,000 $\text{h}^{-1}$	355 (250–450)	[40] 2017
0.05% Pd-Co/ $\text{Al}_2\text{O}_3$ (0.3% Co) $212 \text{ m}^2 \text{ g}^{-1}$	0.01% $\text{CH}_4$ , 1% $\text{H}_2\text{O}$ in air 60,000 $\text{h}^{-1}$	360 (300–500)	[33] 2015
MnOx(0.13)-NiOx $113 \text{ m}^2 \text{ g}^{-1}$	1% $\text{CH}_4$ , 19% $\text{O}_2$ , Ar balance 32 $\text{NL h}^{-1} \text{ g}^{-1}$	365 (275–470)	[34] 2013
3% Pd/ $\text{Co}_3\text{O}_4$ $6 \text{ m}^2 \text{ g}^{-1}$	2% $\text{CH}_4$ , 8% $\text{O}_2$ , $\text{N}_2$ balance 0.1 $\text{NL min}^{-1}$ 12,000 $\text{h}^{-1}$	370 (275–440)	[35] 2015
2.2% Au/ $\text{Co}_3\text{O}_4$ $33 \text{ m}^2 \text{ g}^{-1}$	0.6% $\text{CH}_4$ in air 100,000 $\text{h}^{-1}$	380 (275–550)	[37] 2013
1% Pd/ $\text{Co}_3\text{O}_4$ $6 \text{ m}^2 \text{ g}^{-1}$	0.5% $\text{CH}_4$ , 2% $\text{O}_2$ , $\text{N}_2$ balance 0.1 $\text{NL min}^{-1}$ 12,000 $\text{h}^{-1}$	390 (320–460)	[36] 2016
3% (Pd + Co)/ $\text{Al}_2\text{O}_3$ Pd:Co = 1:1	0.4% $\text{CH}_4$ , 10% $\text{O}_2$ , $\text{N}_2$ balance 0.1 $\text{NL min}^{-1}$ 300 $\text{h}^{-1}$	425 (300–550)	[41] 2015
MnOx-CeO <sub>2</sub> (70 mol% of MnO <sub>2</sub> ) $62 \text{ m}^2 \text{ g}^{-1}$	1% $\text{CH}_4$ , 5% $\text{O}_2$ , He balance 0.04 $\text{NL min}^{-1}$ 0.03 $\text{h}^{-1}$	435 (310–590)	[38] 2015
La(Mn,Pd)O <sub>3</sub> 2.9 wt.% Pd $12 \text{ m}^2 \text{ g}^{-1}$	1% $\text{CH}_4$ , 4% $\text{O}_2$ , He balance 0.1 $\text{NL min}^{-1}$ 60,000 $\text{h}^{-1}$	485 (300–600)	[39] 2013
2% Pd/BaCeO <sub>3</sub> · 2ZrO <sub>2</sub> $26.4 \text{ m}^2 \text{ g}^{-1}$	2% $\text{CH}_4$ , 16% $\text{O}_2$ , He balance 0.05 $\text{NL min}^{-1}$ 6,000 $\text{h}^{-1}$	510 (270–620)	[28] 2015

based on the SSA were calculated taking the  $\text{Co}_3\text{O}_4$  density equal to  $6.1 \text{ g cm}^{-3}$ .

Field-emission scanning electron microscopy (FESEM JEOL-JSM-6700F instrument) was performed to analyze the morphology of the selected spinel samples with and without Pd.

The relative content of cobalt and palladium metals in the investigated catalysts, in the form of pressed discs, 10 mm in diameter, was determined with the use of Energy-Dispersive XRF spectrometer (Thermo Scientific, ARL QUANT'X). The X-rays of 4–50 kV (1 kV step) with the beam size of 1 mm were generated with the Rh anode. The detector used was a 3.5 mm Si(Li) drifted crystal with a Peltier cooling ( $\sim 185 \text{ K}$ ). For quantitative analysis, the calibration with a series of metallic standards and a UniQuant software were used.

X-ray photoelectron spectroscopy (XPS) was performed to determine the surface elemental composition of the catalysts samples. The analysis was carried out using a Physical Electronics PHI 5800 Versa Probe electron spectrometer system with monochromated Al K X-ray source at 1486.60 eV operated at 25 W, 15 kV, with  $100 \mu\text{m}$  X-rays spot. A dual beam charge neutralization method was applied, combining both low energy ions and electrons, to reduce any possible charging effects of X-rays. Prior the measurement the samples were outgassed in an ultrahigh vacuum chamber at  $2.5 \times 10^{-6} \text{ Pa}$  for 12 h. Survey scans were recorded from 0 to

1200 eV. The high-resolution O 1 s spectra were collected from 523 to 543 eV, Co 2p from 765 to 815 eV, C 1s from 278 to 298 eV, and Pd 3d from 330 to 350 eV. All the spectra were obtained under identical conditions, with the samples placed in an ultrahigh vacuum chamber, and calibrated against a value of the C 1s binding energy of 284.5 eV, with a standard deviation equal to 0.3 eV.

#### 2.4. Temperature programmed tests

$\text{H}_2$ -TPR tests were performed using a Quantachrome ChemBET Pulsar TPR-TPD instrument with a TCD detector, using 5%  $\text{H}_2/\text{Ar}$  with flow rate  $15 \text{ NmL min}^{-1}$  and heating rate  $5 \text{ }^\circ\text{C min}^{-1}$ . For each test, the catalyst mass was 30 mg. The experiments were carried out in a quartz U-tube in the temperature range from 25 to  $700 \text{ }^\circ\text{C}$ , with a heating rate  $15 \text{ }^\circ\text{C min}^{-1}$ . A cold trap between the cell and the detector was used to remove water vapor from the  $\text{Co}_3\text{O}_4$  reduction.

The catalytic activity toward  $\text{CH}_4$  combustion (temperature programmed oxidation,  $\text{CH}_4$ -TPO) of the investigated catalysts was tested in a lab-scale fixed-bed micro-reactor (U-shape quartz tube with 4 mm ID). The micro-reactor was filled with 0.1 g of catalyst (0.4–0.6 mm in size) mixed with 0.9 g of  $\text{SiO}_2$  (0.2–0.7 mm in size), sandwiched between two quartz wool layers, to prevent the catalytic bed clogging. The micro-reactor, placed into a PID-

regulated electrical oven, was fed with  $0.1 \text{ NL min}^{-1}$  of a gaseous mixture containing 2 vol.%, 1 vol.%, or 0.5 vol.%  $\text{CH}_4$  in  $\text{N}_2$ , with an excess of oxygen. Precisely, the oxygen-to-methane ratio was fixed equal to 8 for all the reaction conditions, equal to an oxygen-to-methane equivalence ratio  $\lambda$  of 4, considering 2 as a stoichiometric oxygen-to-methane ratio ( $\lambda = (\text{oxygen-to-methane})_{\text{actual}} / (\text{oxygen-to-methane})_{\text{stoichiometric}}$ ). The micro-reactor temperature was measured by a K-type thermocouple placed inside the catalytic bed.  $\text{CH}_4$ -TPO tests were performed by increasing the temperature of the micro-reactor up to  $700^\circ\text{C}$  ( $50^\circ\text{C min}^{-1}$ ) in an  $\text{N}_2$  stream ( $0.1 \text{ NL min}^{-1}$ ), then switching the feed to the reactive stream ( $\text{CH}_4/\text{O}_2/\text{N}_2$  in the desired amounts,  $0.1 \text{ NL min}^{-1}$ , equivalent to  $12,000 \text{ h}^{-1}$  as gas hourly space velocity) until the  $\text{CH}_4$  combustion was complete. When this condition was reached, the oven was allowed to cool naturally ( $\sim 5^\circ\text{C min}^{-1}$ ). During the oven cooling phase, the reactor outlet dry gas concentrations were measured as a function of the temperature. The gas phase concentrations were measured with a continuous ABB analyzer equipped with an NDIR module Uras 14 for  $\text{CO}/\text{CO}_2/\text{CH}_4$  and with a paramagnetic module Magnos 106 for  $\text{O}_2$ . S-shaped curves were obtained by plotting the  $\text{CH}_4$  conversion ( $X$ ) versus the temperature. To guarantee the repeatability of the results, the testing procedure consisted in testing each catalyst three times per each inlet methane concentration, in the order 2, 1, and 0.5 vol.%, and repeating again the 2 vol.% to check the absence of any decay in activity because of the high temperature of exposure during the combustion reaction. The light-off temperature ( $T_{10}$ ) and the half-conversion temperature ( $T_{50}$ ) were regarded as indexes of the catalytic activity of each investigated catalyst. Further analysis of the samples' reactivity was performed on the basis of their reaction rates determined at  $350^\circ\text{C}$ . The reaction rates were determined per  $\text{m}^2$  of the catalyst,  $r_{\text{SSA}}$  ( $\mu\text{mol CH}_4 \text{ m}^{-2} \text{ s}^{-1}$ ), per g of Pd averaged over the whole sample (derived from XRF),  $r_{\text{Pd(XRF)}}$  ( $\mu\text{mol CH}_4 \text{ g}_{\text{Pd(XRF)}}^{-1} \text{ s}^{-1}$ ), and per Pd content proportional to surface exposed Pd-species, from the XPS analysis,  $r_{\text{Pd(XPS)}}$  ( $\mu\text{mol CH}_4 \text{ g}_{\text{Pd(XPS)}}^{-1} \text{ s}^{-1}$ ). The following formulas were used for reaction rates calculation:

$$r_{\text{SSA}} = \frac{F_{\text{CH}_4}}{\text{SSA}} \cdot X \cdot 10^6 \quad (1)$$

$$r_{\text{Pd}} = \frac{F_{\text{CH}_4}}{m_{\text{Pd}}} \cdot X \cdot 10^6 \quad (2)$$

where  $F_{\text{CH}_4}$  ( $\text{mol s}^{-1}$ ) is the molar flow rate of the methane, and  $m_{\text{Pd}} = \text{Pd} \cdot m_{\text{sample}}$  (g), with the Pd% content determined either by XRF or XPS analysis.

Since the catalytic tests were not optimized to determine intrinsic kinetic data (reaction constant, activation energy), the calculated reaction rates are used as non-intrinsic kinetic parameters (not true kinetic data) to facilitate direct comparison of the catalysts. As the same loading catalyst was put into the reactor, the conversion curves are proportional to the mass activity of the catalysts. Moreover, the wide temperature range of the observed catalytic activity also prevents from using the obtained data for true kinetic comparison.

### 3. Results

#### 3.1. Optimization of fuel-to-oxidizer ratio for the undoped $\text{Co}_3\text{O}_4$

Since the unpromoted  $\text{Co}_3\text{O}_4$  spinel material exhibits catalytic activity in the  $\text{CH}_4$  total oxidation, before the palladium doping a synthesis optimization of cobalt spinel was performed. Different fuel-to-oxidizer ratios ( $\phi$ ) were examined: 1.25, 1.00, 0.75, 0.50, and 0.25. For this set of samples, only the basic characterization was performed. All materials were pure phase  $\text{Co}_3\text{O}_4$ , as depicted in Fig. 1, with the typical diffraction maxima of  $\text{Fd}3\text{m}$   $\text{Co}_3\text{O}_4$ . The

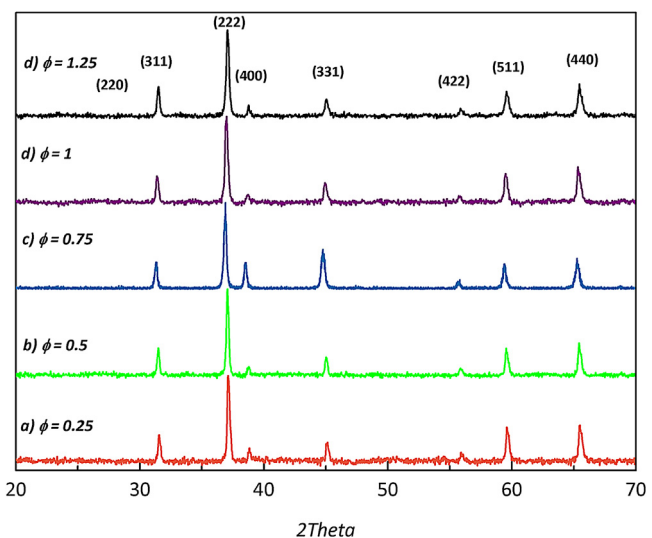
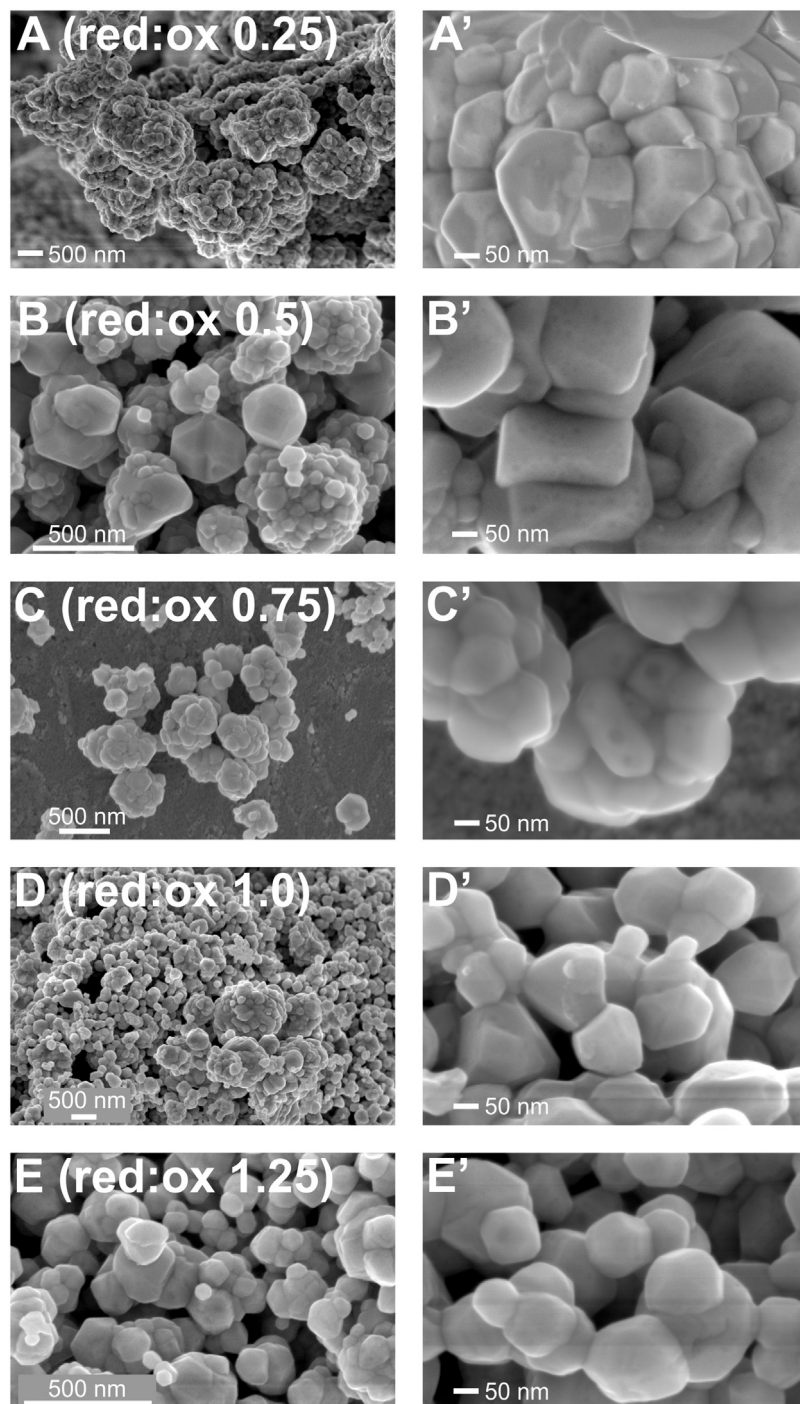


Fig. 1. X-ray diffractograms of the  $\text{Co}_3\text{O}_4$  spinel samples obtained by SCS with different fuel-to-oxidizer ratio,  $\phi$ .

Scherrer equation was used for the  $\text{Co}_3\text{O}_4$  particles diameter calculation,  $D_{\text{XRD}}$  (as reported in Fig. 4).

Representative FESEM pictures of the cobalt spinel materials synthesized with different fuel:oxidizer ratios are presented in Fig. 2A-E. In the micron scale, the morphology changes are evident when passing from red:ox 0.25 to 1.25. From a loose collection of crystals agglomerates (A), a sponge-like structure is gradually formed, and become very well developed for the highest red:ox ratio (Fig. S1 in the Supplementary content). In the submicron scale, for red:ox value 0.25, Fig. 2A,A', the material is composed of large ( $\sim 1.5 \mu\text{m}$ ), spherical agglomerates of primary particles ( $\sim 50$ – $200 \text{ nm}$ , various shapes). When the amount of oxidizer is increased to red:ox 0.5, Fig. 2B,B', the agglomerates' size decreases to  $300$ – $500 \text{ nm}$ , and the primary particle size decreases to  $50$ – $100 \text{ nm}$ . Additionally, large, well-formed crystals of  $150$ – $200 \text{ nm}$  in diameter become an important constituent of the material. For the red:ox 0.75 sample, the dominating features are aggregates of  $300$ – $500 \text{ nm}$  (Fig. 2C,C'). In the case of a stoichiometric mixture, red:ox 1.0, the large spherical aggregates are still there, but the remaining crystals are smaller,  $\sim 100 \text{ nm}$ , and constitute the larger part of the material (Fig. 2D,D'). The decreasing trend of the agglomeration and decrease of the individual particle sizes continues for catalyst red:ox 1.25, where relatively small, well dispersed individual crystals constitute the catalyst (Fig. 2E,E'). The BET specific surface area values for fuel-to-oxidizer ratios ( $\phi$ ) 0.25, 0.50, 0.75, 1.00, and 1.25 were  $1.2, 2.4, 2.7, 2.9$ , and  $2.4 \text{ m}^2 \text{ g}^{-1}$ , respectively.

Fig. 3A–C shows the catalytic activity of these materials as  $\text{CH}_4$  conversion curves for different  $\text{CH}_4$  inlet concentrations. The only products formed during the combustion were water (removed prior entering the analyzer in a condenser settled at  $3^\circ\text{C}$ ) and carbon dioxide. No carbon monoxide was detected in the reactor effluent mixture, in agreement with the high inlet working lambda value. Interestingly, all catalysts behave in a very similar way, with few differences among the various  $T_{50}$ , almost independent on the inlet methane concentration. Apparently, the structural characteristics of the various spinels do not affect the methane combustion in lean conditions. For the lowest methane concentration used, 0.5 vol.%, the highest activity belongs to the spinel catalyst obtained with the stoichiometric reaction mixture ( $\phi = 1.0$ ), Fig. 3A. In the case of 1 vol.% methane concentration, the temperature range of exhibited activities is very similar for all the catalysts, Fig. 3B, with the highest activity reached by the spinel with  $\phi = 0.75$ . For 2 vol.%  $\text{CH}_4$ , the



**Fig. 2.** FESEM images of the  $\text{Co}_3\text{O}_4$  spinel samples obtained by SCS with fuel-to-oxidizer ratio, red:ox, from 0.25 to 1.25, at different magnifications; A–E: lower, A'–E': higher magnification.

most active  $\text{Co}_3\text{O}_4$  material was obtained with sub-stoichiometric fuel:oxidizer  $\phi$  ratio equal to 0.75, **Fig. 3C**. The reaction temperature window is broader in this case, and the optimal reactivity for red:ox 0.75 is clearly visible. **Fig. S2** in the Supplementary content better enlightens the variations of the  $T_{50}$  in the various reaction conditions.

To choose the best operative conditions in terms of fuel:oxidizer ratio to produce Pd-promoted  $\text{Co}_3\text{O}_4$  catalysts, we compared the catalytic activity ( $T_{50}$ ), the reaction enthalpy during the SCS, the adiabatic flame temperature reached during the SCS, and the particles diameter of the  $\text{Co}_3\text{O}_4$  catalysts from XRD, as shown in **Fig. 4** for the

2 vol.%  $\text{CH}_4$  inlet concentration (the case where the increase of the catalytic activity was more evident). The following formulas were used for reaction enthalpy and the adiabatic flame temperature calculations:

$$\Delta H_r = \Delta H_p^0 - \Delta H_r^0 \quad (3)$$

$$T = T_r - \frac{\Delta H_r}{C_p} \quad (4)$$

Where  $T_r$  is the temperature of reaction ( $250^\circ\text{C}$ ),  $\Delta H_r^0$  and  $\Delta H_p^0$  are the enthalpies of formation of reactant and products and  $C_p$  is the heat capacity of the products at constant pressure. **Table 2**

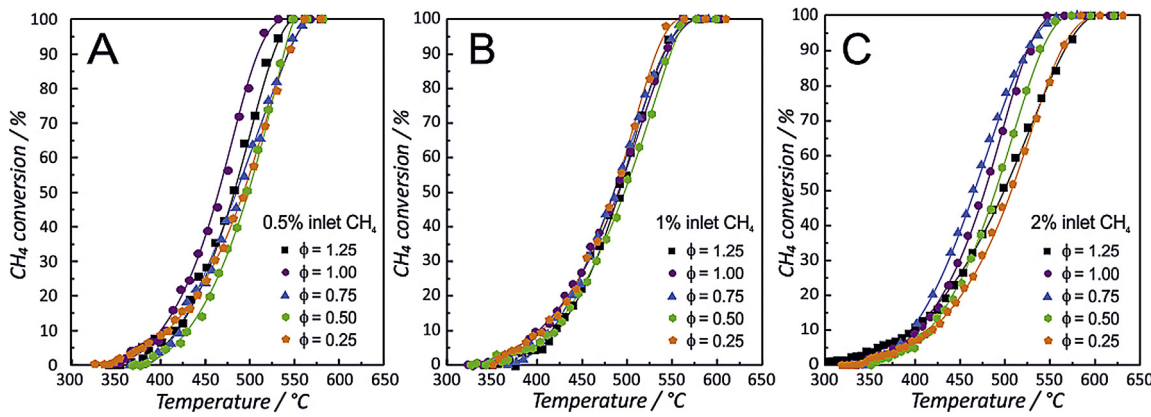


Fig. 3. CH<sub>4</sub>-TPO profiles for Co<sub>3</sub>O<sub>4</sub> spinel catalysts obtained by SCS with different fuel-to-oxidizer ratio. A) 0.5 vol.% inlet CH<sub>4</sub>, B) 1 vol.% inlet CH<sub>4</sub>, C) 2 vol.% inlet CH<sub>4</sub>.

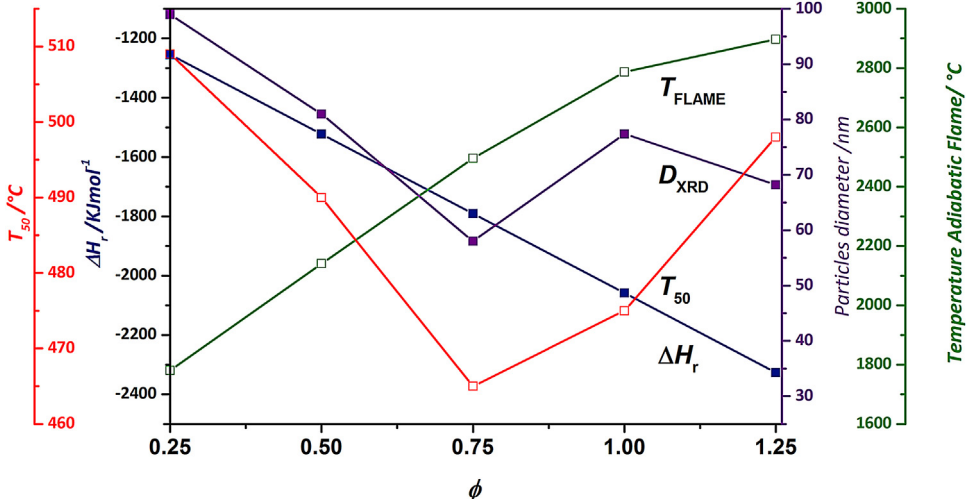


Fig. 4. Calculated reaction enthalpies  $\Delta H_r$  and adiabatic flame temperatures  $T_{FLAME}$  along with reactivity data,  $T_{50}$  (for 2 vol.% inlet CH<sub>4</sub>), and crystal sizes from XRD for Co<sub>3</sub>O<sub>4</sub> spinel catalysts obtained by SCS with different fuel-to-oxidizer ratio.

Table 2

Thermodynamic parameters for calculation of the reaction enthalpies and the adiabatic flame temperatures with different red:ox ratios.

Compound	$\Delta H_r$ kJ mol <sup>-1</sup>	$C_p$ kJ mol <sup>-1</sup> K <sup>-1</sup> (#)
Co(NO <sub>3</sub> ) <sub>2</sub> ·6H <sub>2</sub> O (s)	-464.94	-
NH <sub>2</sub> CH <sub>2</sub> COOH (s)	-393.609	-
Co <sub>3</sub> O <sub>4</sub> (s)	-0.097	5510087 + 0.2767 $T$
CO <sub>2</sub> (g)	-393.697	43.283 + 0.0114 $T$
N <sub>2</sub> (g)	0	27.209 + 0.0114 $T$
O <sub>2</sub> (g)	0	24.781 + 0.0153 $T$
H <sub>2</sub> O (g)	-241.934	30.139 + 0.015 $T$

(#)  $T$  – reaction temperature.

lists the available thermodynamic data taken from [54,55] for the reactants and products.

The particles diameter,  $D_{XRD}$ , and the  $T_{50}$  show a minimum for the red:ox 0.75, Fig. 4. It is clear that for these cobalt spinel series the smaller the particles diameter the better the catalytic activity. When the red:ox ratio is increased from 0.25 to 1.25, the amount of gasses produced, the reaction enthalpy, and the adiabatic flame temperature also increase, as reported in Fig. 4. Therefore, on the one hand the increased volume of gasses potentially lead to an increased porosity, but on the other the reaction temperature also increases, enhancing the sintering of the synthesized material. Thus, it is reasonable to conclude that at red:ox ratio 0.75 optimal conditions are reached for the most dispersed cobalt spinel. Since

the SSA values for this series of materials pass through a maximum for red:ox 0.75–1.00 (2.7–29 m<sup>2</sup> g<sup>-1</sup>), the smallest  $D_{XRD}$  for red:ox 0.75 unambiguously points out this material as most promising support for hosting the palladium phase. Moreover, by performing a quick estimate of the economy of the synthesis process of the Co<sub>3</sub>O<sub>4</sub> spinel, urea as a commodity has an average price that ranged from 177 to 214 US\$ per metric ton in the year 2016 [56,57]. Consequently, the lower the  $\phi$  ratio, the lower the amount of the starting precursor, the better the economy of production.

### 3.2. Optimization of Pd content for Co<sub>3</sub>O<sub>4</sub> doping

#### 3.2.1. Specific surface area, phase composition and crystal sizes

The 0.75 stoichiometry was selected for Pd-doping based on the previous results from the optimization of the fuel-to-oxidizer ratio for undoped Co<sub>3</sub>O<sub>4</sub>. We chose Pd amounts of 0.5, 1, 1.5, 3, and 5 wt.%, to cover the range of acceptable precious metal quantities. The synthesis of the Pd-doped spinels consisted of an additional step of Pd-impregnation and subsequent calcination compared to the synthesis of the sole spinels. The SSA slightly increased due to the palladium doping, despite the second calcination of the spinel catalyst, Table 3. For all the Pd-doped catalysts, the SSA values were in the range of 4–6 m<sup>2</sup> g<sup>-1</sup>.

Similarly to the unpromoted catalysts, the cobalt spinel was the main phase detected by XRD, Fig. 5. Only for the 3% and 5%

**Table 3**

Pd content, specific surface areas and calculated grain sizes from  $N_2$ -BET ( $D_{SSA}$ ) and crystal sizes from XRD of cobalt spinel support for palladium doped catalysts.

Pd nominal content/%	Pd content (XRF)/wt.%	$SSA(Co_3O_4)/m^2 g^{-1}$	$D_{SSA}(Co_3O_4)/nm$	$D_{XRD}(Co_3O_4)/nm$
0	–	2.7	70	58
0.5%	0.3	4.3	229	81
1%	0.79	4.4	224	83
1.5%	1.09	4.8	205	92
3%	2.9	5.1	193	98
5%	4.45	5.9	167	71

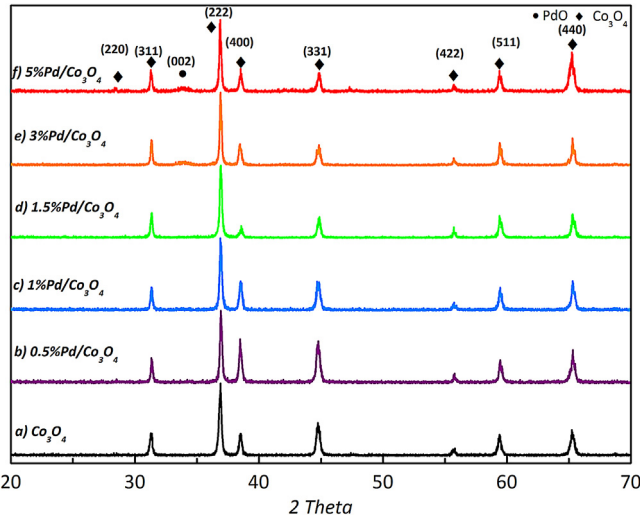


Fig. 5. X-ray diffractograms of the  $Co_3O_4$  spinel catalysts doped with palladium in the range of 0–5 wt.%; ♦ –  $Co_3O_4$  phase, ● – PdO phase.

Pd/ $Co_3O_4$  catalysts, a broad, weak diffraction peak at  $33.601^\circ$  2 $\theta$ , assigned to PdO (002) starts to appear. The crystal sizes of the spinel phase calculated with the Scherrer equation,  $D_{XRD}$ , are similar for all impregnated Pd/ $Co_3O_4$  catalysts and are in the range 70–100 nm. On the other hand, the  $D_{SSA}$  values estimated for selected catalysts show that large parts of the surfaces of the crystals are inaccessible for adsorption leading to the grains sizes in the range 170–230 nm (Table 3).

### 3.2.2. Catalytic tests

Fig. 6 shows the comparison of the catalytic activity toward the methane combustion reaction (conversion vs. temperature) of the prepared catalysts, for different  $CH_4$  inlet concentrations: 0.5, 1.0, and 2.0 vol.%. Considering the testing procedure, each catalysts

was tested ten times, showing very good reproducibility results and no deactivation effects (average time on stream for each catalyst: 20 h). Fig. S3 in the Supplementary content better enlightens the S-shaped curves of the activity for each catalyst in the various reaction conditions. Similarly to the unpromoted catalysts, the only products formed during the combustion were water and carbon dioxide. Again, no carbon monoxide was detected in the reactor effluent mixture, because of the high inlet working lambda value. Moreover, catalysts behave in a very similar way, independently on the inlet methane concentration (Fig. S3). The improvement in the catalytic activity depends mainly on the Pd-loading (Fig. 6). In fact, for every  $CH_4$  concentration, the unpromoted  $Co_3O_4$  was the least active catalyst. For the 0.5 and 1 vol.%  $CH_4$  concentrations, the most active one was the 5% Pd/ $Co_3O_4$  while the most active catalyst was the 3% Pd/ $Co_3O_4$  for the highest  $CH_4$  concentration. For convenience, Fig. S4 in the Supplementary content shows the effect of Pd doping on the  $T_{10}$  and  $T_{50}$  of the unpromoted  $Co_3O_4$  (delta values). Further reactivity data analysis is available in the discussion section.

To understand the effect of Pd loading on the catalytic activity of Pd/ $Co_3O_4$  materials an in-depth characterization was performed for the four selected catalysts: undoped  $Co_3O_4$ , 1 wt.% Pd, 3 wt.% Pd, and 5 wt.% Pd catalysts.

### 3.2.3. Structural Raman characterization

The Raman spectra of  $Co_3O_4$  and palladium promoted  $Co_3O_4$  reveal five main Raman peaks, Fig. 7. These peaks are located near 188, 470, 512, 606, and  $675\text{ cm}^{-1}$ , and correspond to the  $F_{2g}$ ,  $E_g$ ,  $2\times F_{2g}$  and  $A_{1g}$  modes of crystalline  $Co_3O_4$ , respectively [58]. For the cobalt-only spinel phase obtained with the SCS method, an asymmetry of the  $A_{1g}$  band can be observed, as reported previously [35,36]. An additional peak at  $640\text{ cm}^{-1}$  can be observed in Fig. 7E (and more clearly in Fig. S5 in the Supplementary content), which can be assigned to the PdO phase [59]. The evident heterogeneity of the samples, especially in Fig. 7B and C, as evidenced by the presence of two sets of bands cannot be explained

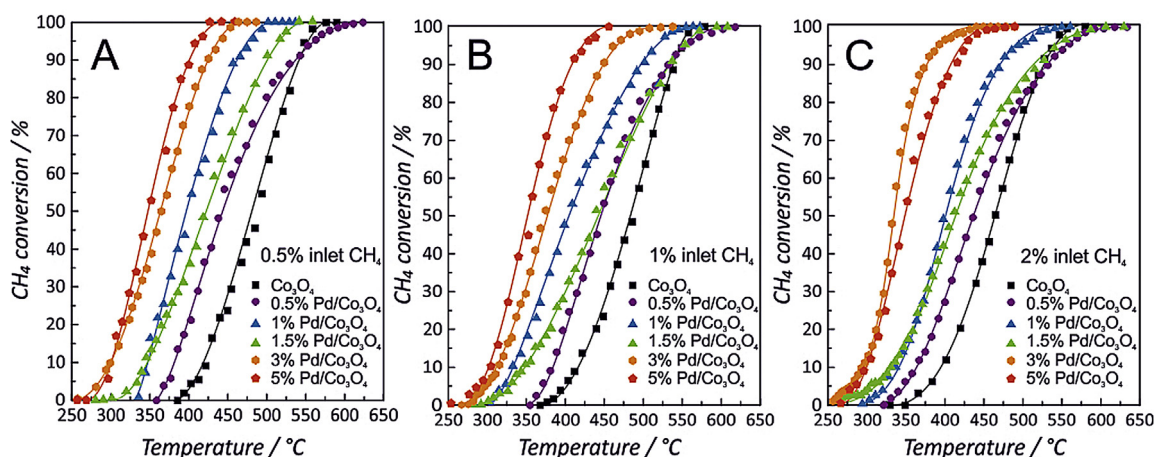
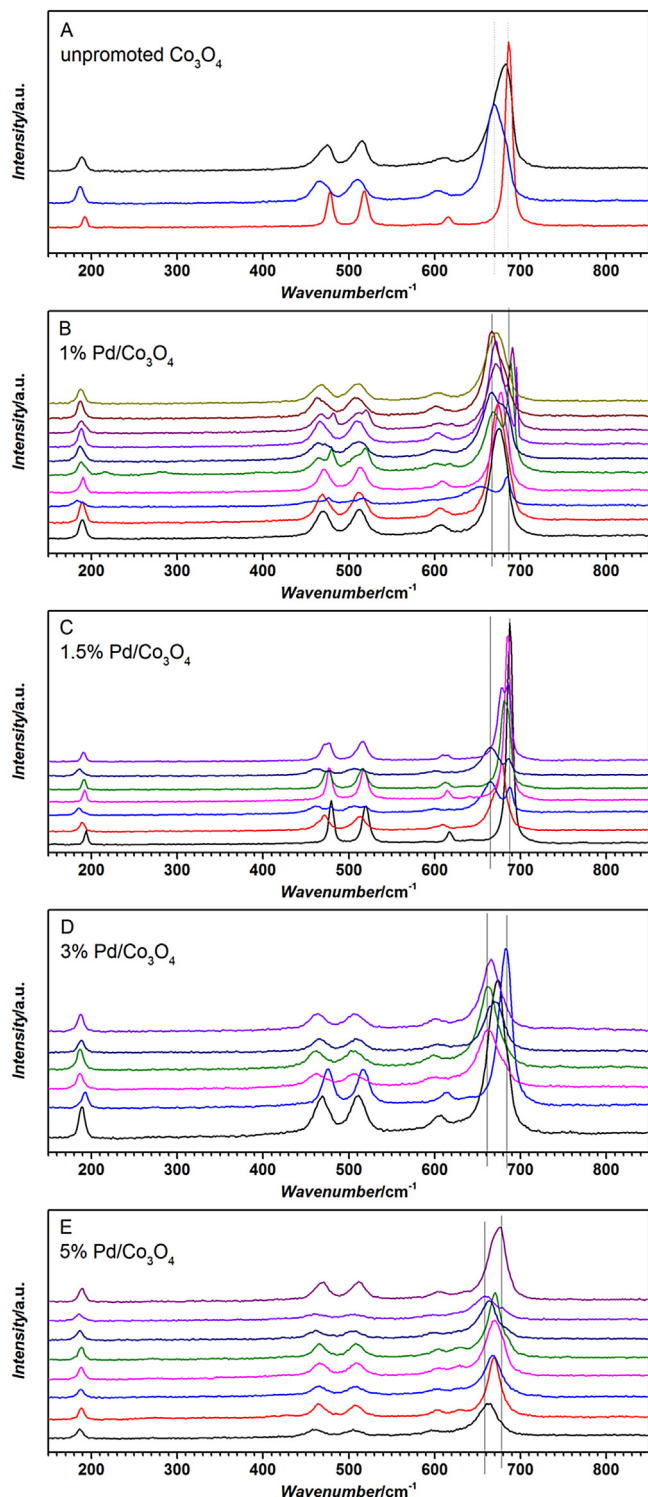
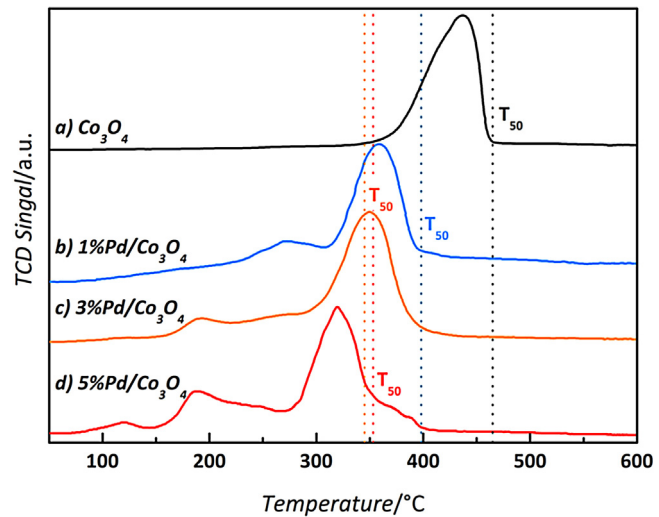


Fig. 6.  $CH_4$ -TPO profiles of the  $Co_3O_4$  spinel catalysts doped with palladium in the range of 0–5 wt.%. A) 0.5 vol.% inlet  $CH_4$ , B) 1 vol.% inlet  $CH_4$ , C) 2 vol.% inlet  $CH_4$ .



**Fig. 7.** Raman spectra of A) unpromoted  $\text{Co}_3\text{O}_4$  red: ox 0.75, and the palladium doped  $\text{Co}_3\text{O}_4$  with B) 1 wt.% Pd, C) 1.5 wt.% Pd, D) 3 wt.% Pd, and E) 5 wt.% Pd. Different curves for the same material represent different spots on the powdered catalyst from which the spectra were taken. (For interpretation of the references to color in this figure legend, the reader is referred to the web version of this article.)

by the local interaction of  $\text{Co}_3\text{O}_4$  with PdO because, as indicated in the experimental part, the minimum spot of the laser is just short of 1  $\mu\text{m}$ . The second reason is that it is also observed for the unpromoted sample, Fig. 7A. The material is polycrystalline with possible two types of crystal types – aggregates of smaller crystals and more loose larger crystals. Thus, some observed shifts of



**Fig. 8.**  $\text{H}_2$ -TPR profiles of the a) undoped  $\text{Co}_3\text{O}_4$  spinel oxide and doped with palladium b) 1 wt.% Pd/ $\text{Co}_3\text{O}_4$ , c) 3 wt.% Pd/ $\text{Co}_3\text{O}_4$ , d) 5 wt.% Pd/ $\text{Co}_3\text{O}_4$ .

the bands' positions without concomitant changes in the spectral band structure (additional peaks, asymmetry) could originate from the non-uniform sample surface and thermal effects due to laser exposure [60], as for unpromoted  $\text{Co}_3\text{O}_4$ . The main observation of Fig. 7 is that the two domains are clearly distinguishable for the low Pd amounts, while the more Pd is in the sample the lower is the contribution of the high wavenumber component. As reported in [36,60,61], the high wavenumber component is typical for non-agglomerated particles (e.g., obtained by the precipitation method), while the low wavenumber component, with much larger FWHM, is typical for agglomerated particles. This effect was investigated by Lorite et al. [60] and can be summarized to be due to i) transmission of the phonons between agglomerated nanoparticles that produce larger Raman bands red-shift and line broadenings and ii) a different temperature dependence of the generation of acoustic phonons of agglomerated and non-agglomerated particles. The studied materials were obtained by the same synthesis procedure, and as evidenced by the FESEM studies (Paragraph 3.2.5) possess, in general, similar morphologies. Thus, the observed effect cannot be due to change of the catalysts' agglomeration state but must be caused by the Pd addition. The presence of the PdO phase thus facilitates heating of the catalysts upon laser irradiation and uniform heat distribution resulting in dominant low wavelength component. The interaction of PdO phase with  $\text{Co}_3\text{O}_4$  may be facilitated by the partial reduction of the cobalt spinel surface, as evidenced by the XPS results (Paragraph 3.2.6) and postulated in our previous works [35,36,62].

### 3.2.4. Temperature programmed reduction

The  $\text{H}_2$ -TPR profile of the unpromoted catalyst is typical for cobalt spinel, with reduction signal maximum spanning from 350 to 430 °C, and a tail towards lower temperatures (Fig. 8). Although a double maximum is usually observed for  $\text{Co}_3\text{O}_4$  [63–65], a one-maximum or asymmetric reduction curves were also reported [66–68]. It is due to a well-known fact that the reduction profile of  $\text{Co}_3\text{O}_4$  greatly depends on the morphology and size of the constituting particles [68,69]. Palladium doping brings about evident changes in the reduction behavior, consistently with the reported data [70]. Firstly, the cobalt oxide reduction maximum is shifted towards lower temperatures. Secondly, new maxima appear on the low-temperature side of the cobalt reduction signal. The positions of the maxima due to cobalt oxide reduction and the new maxima depend on the palladium loading. In general, the higher amount

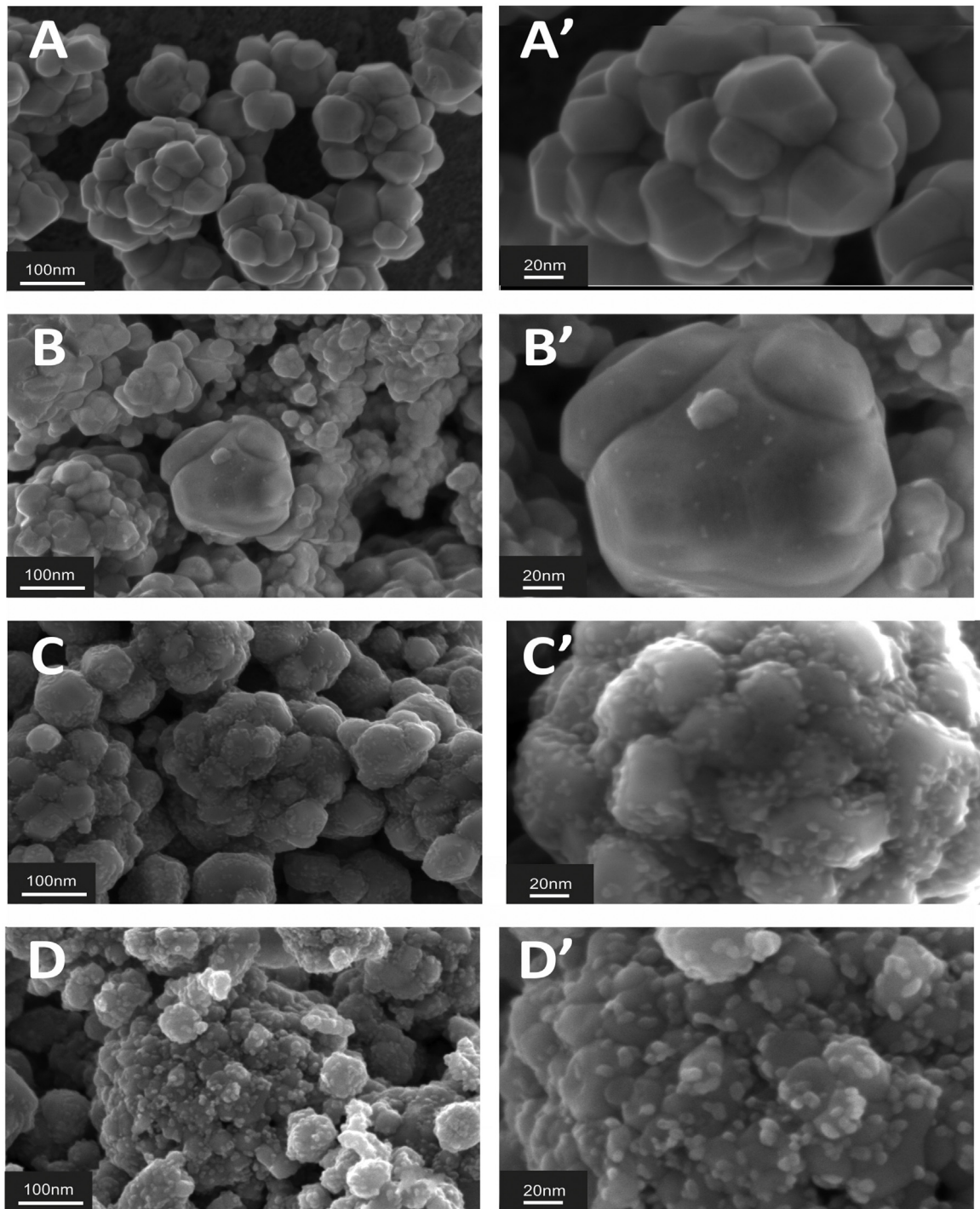


**Fig. 9.** FESEM pictures at different magnifications of the A) undoped  $\text{Co}_3\text{O}_4$  spinel oxide and doped with palladium B) 1 wt.% Pd/ $\text{Co}_3\text{O}_4$ , C) 3 wt.% Pd/ $\text{Co}_3\text{O}_4$ , D) 5 wt.% Pd/ $\text{Co}_3\text{O}_4$ .

of Pd the lower the temperature of the reduction peaks. The additional, low-temperature peaks were assigned to the PdO reduction, and their positions depend on the PdO dispersion [71]. However, because the amount of Pd is relatively low in comparison with Co, the observed intensity of the low-temperature peak may not be entirely due the PdO reduction. It has been reported that a reduction of  $\text{Co}^{3+}$ – $\text{Co}^{2+}$  can be shifted to temperatures around 200 °C, due to the  $\text{H}_2$  spillover effect [71]. Moreover, literature data point out that PdO deposited over zirconia doped ceria can be reduced at temperatures as low as 60 °C [72,73]. Therefore, the weak feature at *c.a.* 120 °C visible in Fig. 8 for 3 and 5% Pd/ $\text{Co}_3\text{O}_4$  catalysts can

be due PdO reduction. Thus, formed metallic Pd then catalyzes the reduction of  $\text{Co}^{3+}$ – $\text{Co}^{2+}$ .

### 3.2.5. FESEM analysis

The microscopic pictures obtained by FESEM depict morphology of the catalysts at different magnifications, Fig. 9. The undoped  $\text{Co}_3\text{O}_4$  nanocrystals are in the size range of 20–80 nm, with the clusters of nanocrystals about 150–300 nm. The crystals are well-developed, exhibiting typical rhombicuboctahedral shapes, with the prevailing of (100) and (111) planes, Fig. 9A,A' [74]. For Pd-doped spinel catalysts (Fig. 9B–D), the original  $\text{Co}_3\text{O}_4$  nanocrystals

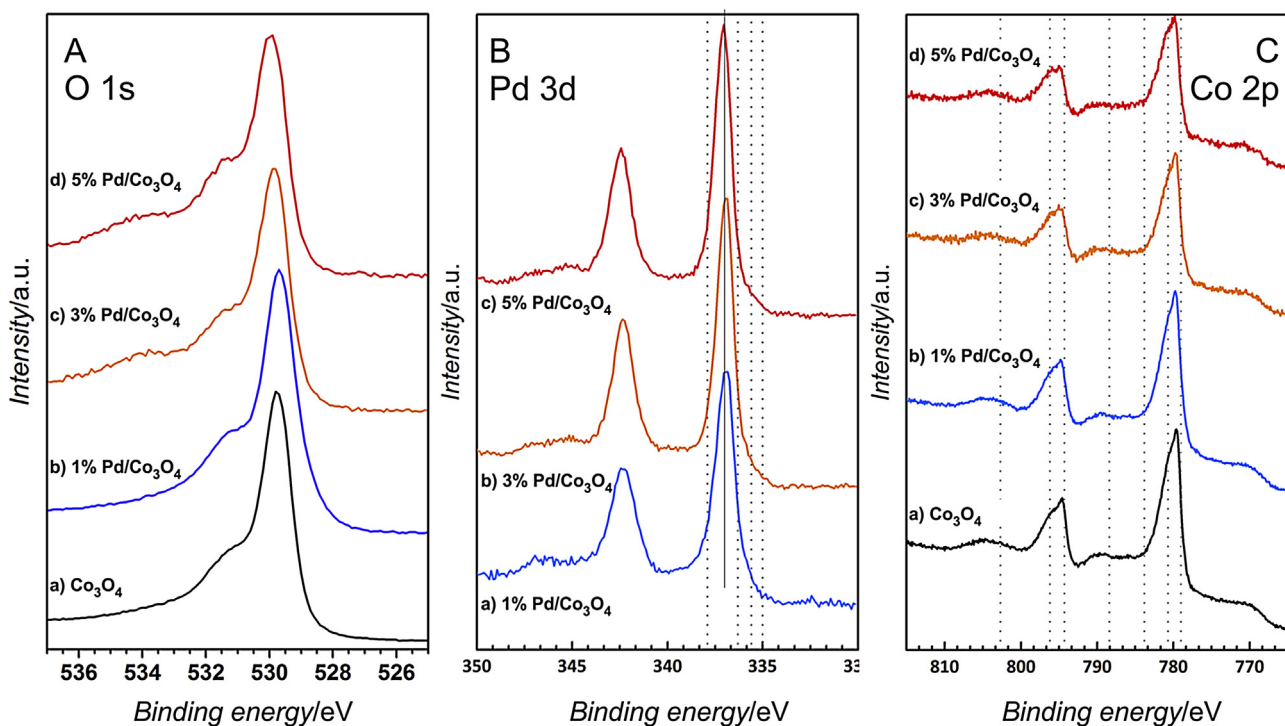


Fig. 10. XPS spectra in the A) O 1s range, B) Pd 3d range and C) Co 2p range for undoped Co<sub>3</sub>O<sub>4</sub> and 1 wt.% Pd/Co<sub>3</sub>O<sub>4</sub>, 3 wt.% Pd/Co<sub>3</sub>O<sub>4</sub> and 5 wt.% Pd/Co<sub>3</sub>O<sub>4</sub>.

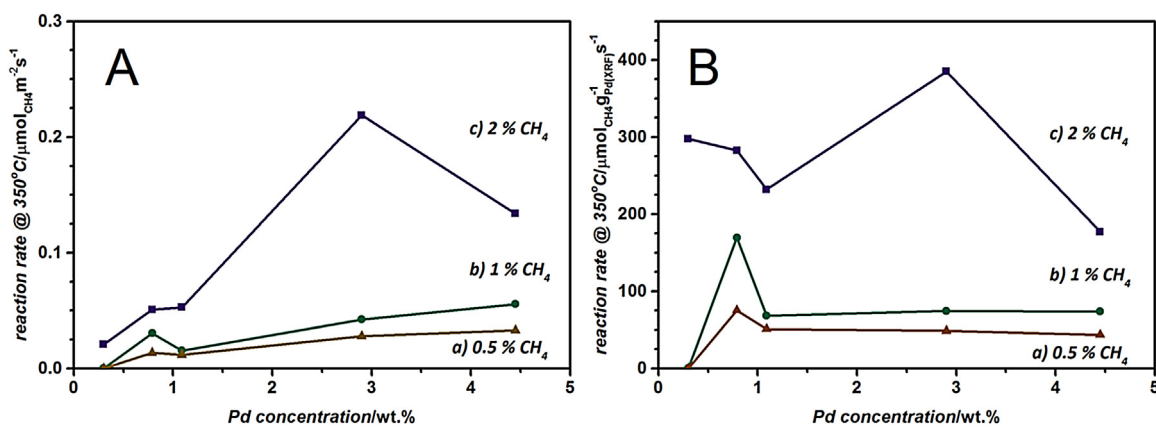


Fig. 11. Reaction rates A) per m<sup>2</sup> based on the SSA values, B) per g<sub>Pd</sub> based on the XRF analysis values, calculated at 350 °C for Co<sub>3</sub>O<sub>4</sub> doped with Pd in the range 0–5 wt.% for a) 0.5 vol.%, b) 1 vol.% and c) 2 vol.% inlet CH<sub>4</sub> concentration.

with the rhombicuboctahedral shapes are preserved, independent on the Pd loading. For the lowest Pd loading (1 wt.%), smaller dots of PdO<sub>x</sub> phase, although rather scarce, are clearly visible. They are well dispersed and very small (<5 nm). The sintering due to the additional calcination step of Co<sub>3</sub>O<sub>4</sub> support is clearly visible (Fig. 9B). Higher Pd loading (3 wt.%) results in a uniform coverage of cobalt spinel surface, but the PdO<sub>x</sub> crystals are larger than for 1 wt.% Pd (<8 nm). The dispersion of PdO<sub>x</sub> nanoparticles is very good, and the formation of agglomerates is limited (Fig. 9C). On the other hand, the increase of Pd level to 5 wt.% results in a clear agglomeration of palladium species and the increase of their crystal sizes (Fig. 9D). Unfortunately, since CO or H<sub>2</sub> chemisorbs on both transition metal oxides on (PdO and Co<sub>3</sub>O<sub>4</sub>), the chemisorption method used to determine metal dispersion over inert supports (Al<sub>2</sub>O<sub>3</sub>, SiO<sub>2</sub>) cannot be used in this case.

Table 4  
Surface composition of the Pd doped samples based on the XPS spectra analysis.

Catalyst	wt.% Co	Co <sup>2+</sup> /(Co <sup>2+</sup> + Co <sup>3+</sup> )	wt.% O	wt.% Pd
Co <sub>3</sub> O <sub>4</sub>	60	0.21	40	–
1% Pd/Co <sub>3</sub> O <sub>4</sub>	53	0.80	32	15
3% Pd/Co <sub>3</sub> O <sub>4</sub>	30	0.80	33	37
5% Pd/Co <sub>3</sub> O <sub>4</sub>	30	0.80	31	39

### 3.2.6. XPS analysis

The undoped Co<sub>3</sub>O<sub>4</sub> support together with the Pd/Co<sub>3</sub>O<sub>4</sub> catalysts with 1, 3, and 5 wt.% Pd loadings were investigated by XPS spectroscopy. Fig. 10 shows the XPS spectra of O 1s, Pd 3d, and Co 2p regions. Table 4 summarizes the surface mass concentrations of Co, O, and Pd.

The O 1s spectra of Co<sub>3</sub>O<sub>4</sub> show two main peaks, Fig. 10A. The peak centered at 529.7 eV is assigned to the lattice O<sup>2-</sup> oxygen

ions, while the second, less intense peak around 531 eV is usually assigned to surface hydroxyl groups, carbonates/adsorbed  $\text{CO}_2$ , etc. [75]. The position of the lattice oxygen peak does not change substantially upon addition of different amounts of palladium. This is not surprising since the O 1s peak for  $\text{PdO}$  is expected around 529–530 eV [51]. For higher amounts of palladium, the additional broad band around 534 eV becomes visible, originating from  $\text{Pd} 3\text{p}$  transition of  $\text{Pd}^{2+}$  ions [76].

The  $\text{Pd} 3\text{d}$  XPS spectra of  $\text{Pd}/\text{Co}_3\text{O}_4$  catalysts consist of two main peaks (Fig. 10B). They are accompanied by weak satellite bands at higher energies. The main  $\text{Pd} 3\text{d}_{5/2}$  band is located at 336.8 eV, in agreement with the literature value of  $\text{Pd}^{2+}$  binding energy [51]. The  $\text{Pd} 3\text{d}$  bands are symmetrical and do not change shape with increasing  $\text{Pd}$  doping level, which indicates that neither  $\text{Pd}^0$  nor  $\text{Pd}^{4+}$  is formed in noticeable quantities. Therefore, it can be concluded that  $\text{Pd}$  exists in the prepared catalysts as  $\text{PdO}$ . The surface composition estimation, listed in Table 3, indicates that  $\text{Pd}$  surface concentration is almost identical for 3%  $\text{Pd}/\text{Co}_3\text{O}_4$  and 5%  $\text{Pd}/\text{Co}_3\text{O}_4$  catalysts. As evidenced by the FESEM pictures, palladium in the 5%  $\text{Pd}/\text{Co}_3\text{O}_4$  catalyst forms agglomerated structures. This effect may cause a shadowing of some  $\text{PdO}$  crystals and render them invisible in the XPS analysis.

The main  $\text{Co} 2\text{p}_{3/2}$  and  $2\text{p}_{1/2}$  lines appear at 780 and 795 eV. The shape and the position of the observed lines are typical for cobalt spinel structure, with no  $\text{CoO}$  phase present at the surface, as shown in Fig. 10C [75]. Should the  $\text{CoO}$  be present, a well-developed satellite structure at 786 eV would be visible with relatively high intensity in comparison with the  $\text{Co} 2\text{p}_{3/2}$  band [75]. The positions of the main bands and their overall intensity, as well as the presence and intensity of the satellite bands, do not change noticeably upon  $\text{Pd}$  doping. The decomposition of the  $\text{Co} 2\text{p}_{3/2}$  band into the components originating from  $\text{Co}^{2+}$  (band at 780.6 eV) and  $\text{Co}^{3+}$  (band at 779.6 eV) revealed, however, substantial differences in the surface cobalt oxidation state. Table 4 lists the collected values. Fig. S6 in the Supplementary content shows the figures with the decomposition of the  $\text{Co} 2\text{p}$  energy range. For the undoped  $\text{Co}_3\text{O}_4$ , the  $\text{Co}^{2+}/(\text{Co}^{2+} + \text{Co}^{3+})$  ratio equals 0.21, which is well below the theoretical value, 0.67. Low  $\text{Co}^{2+}$  amounts may result from the sub-stoichiometric amount of fuel (urea) during the combustion synthesis equal to 0.75. Interestingly, irrespective of the added  $\text{Pd}$  amount, the  $\text{Co}^{2+}/(\text{Co}^{2+} + \text{Co}^{3+})$  ratio increases to 0.80. Since palladium is deposited from an acid solution (oxidizing properties), and the impregnated catalysts were subsequently calcined (oxidative atmosphere), the increase of the reduced cobalt state is bound to be due interaction with  $\text{Pd}$  species.

#### 4. Discussion

Fig. 11A and B shows the specific activity of the catalysts at 350 °C per  $\text{m}^2$  of the catalyst and per  $\text{g}_{\text{Pd}}$  derived from the XRF as a function of palladium content. In general, the reactivity per  $\text{m}^2$  increases monotonically, except for the 3%  $\text{Pd}/\text{Co}_3\text{O}_4$  for higher

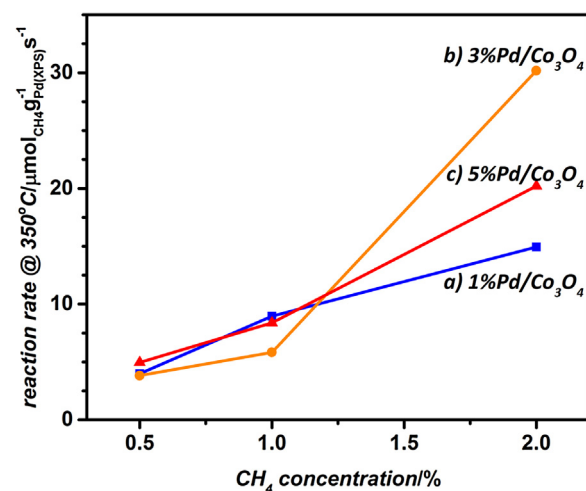


Fig. 12. Reaction rates calculated per  $\text{g}_{\text{Pd}}$  based on the XPS analysis values (surface palladium), calculated at 350 °C for  $\text{Co}_3\text{O}_4$  doped with a) 1, b) 3 and c) 5 wt.%.

methane concentration. On the other hand, the reactivity values per  $\text{g}_{\text{Pd}}$  (XRF) show maxima for 1%  $\text{Pd}/\text{Co}_3\text{O}_4$  and 3%  $\text{Pd}/\text{Co}_3\text{O}_4$  catalysts for lower and higher methane concentrations, respectively. However, no clear trend can be observed in relation to the  $\text{Pd}$  amount. From the bulk characterization techniques (XRD,  $\text{H}_2$ -TPR, XRF) and FESEM, it was established that the nominal 5%  $\text{Pd}/\text{Co}_3\text{O}_4$  catalyst indeed contains more palladium than 3%  $\text{Pd}/\text{Co}_3\text{O}_4$  one. In the same time, the XPS results indicate that the surface  $\text{Pd}$  concentration in both catalysts is very similar (Table 4). Moreover, the surface concentration of palladium (XPS) is 10–20 times higher than the sample averaged  $\text{Pd}$  content (XRF).

Fig. 12 shows the specific activities of 1, 3, and 5%  $\text{Pd}/\text{Co}_3\text{O}_4$  catalysts at 350 °C per  $\text{g}_{\text{Pd}}$  derived from the XPS as a function of methane concentration. At low  $\text{CH}_4$  concentrations, catalysts show very similar reactivity per  $\text{g}_{\text{Pd}}(\text{XPS})$ . The biggest differences can be observed for the 2 vol.% methane concentration, where the most active catalyst is the one with nominal 3%  $\text{Pd}/\text{Co}_3\text{O}_4$  composition. From the FESEM pictures, it was concluded that this catalyst exhibits a more dispersed state of  $\text{PdO}$  particles than the 5%  $\text{Pd}/\text{Co}_3\text{O}_4$  one. A part of the  $\text{PdO}$  crystals in 5%  $\text{Pd}/\text{Co}_3\text{O}_4$  is not seen by the XPS, possibly due to an increased surface roughness and shading effect. The Raman spectroscopic results point out to the more uniform, catalyst averaged interaction of  $\text{PdO}$  phase with  $\text{Co}_3\text{O}_4$  support for higher amounts of  $\text{PdO}$ , resulting in more effective energy transfer through lattice vibrations. The 3%  $\text{Pd}/\text{Co}_3\text{O}_4$  catalyst behave in a similar way under laser irradiation to the 5%  $\text{Pd}/\text{Co}_3\text{O}_4$  but without evidence of the  $\text{PdO}$  phase presence.

Taking the above results into consideration a simple model which accounts for the observed reactivity trends can be proposed. The rate determining step in the low-temperature methane combustion is the C–H bond activation over the  $\text{PdO}$  phase, which

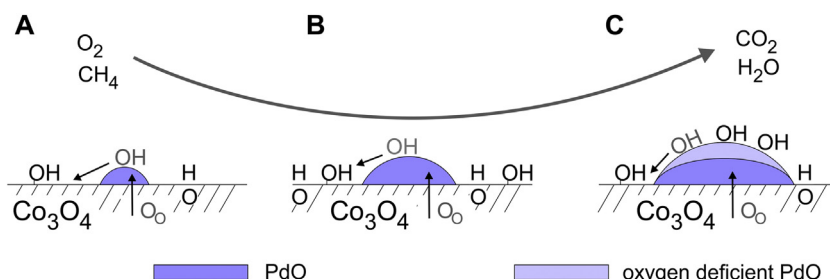


Fig. 13. Proposed reaction scheme for A) low  $\text{PdO}$  content, B) optimum  $\text{PdO}$  content with good dispersion and C) agglomerated  $\text{PdO}$  crystals leading to the inefficient regeneration of active sites.

involves both surface palladium and oxygen ions [77]. However, the reaction can be inhibited by adsorption of oxygen and water molecules [5,78]. Surface hydroxyls resulting from methane combustion impede surface reoxidation, leading to a certain degree of catalyst deprivation of oxygen and formation of bulk oxygen vacancies in PdO, which can be refilled with oxygen from the support, as observed in the literature [79,80]. The support's surface also plays an important role in this reaction, in particular,  $\text{Co}_3\text{O}_4$  which exhibits some catalytic activity even without Pd addition. The interaction of PdO nanocrystals with  $\text{Co}_3\text{O}_4$  support depends on the crystal morphology of cobalt spinel [52] and has been suggested to involve the formation of  $\text{CoOOH}$  surface species [29]. Cobalt spinel may thus act as a sink for hydroxyl species formed on the PdO surface. Therefore, the vicinity of a cobalt oxide phase favors regeneration of active sites on PdO both by accommodation of hydroxyl species and lattice oxygen supply. The oxygen supply could be facilitated by the increase of  $\text{Co}^{2+}$  surface concentration, as evidenced by XPS measurements, due to the simultaneous increase in the concentration of oxygen vacancies, and thus increased the mobility of oxygen in the  $\text{Co}_3\text{O}_4$  subsurface layer. The main difference between 3% Pd/ $\text{Co}_3\text{O}_4$  and 5% Pd/ $\text{Co}_3\text{O}_4$  catalysts is the reactivity in the feed with the highest  $\text{CH}_4$  concentration. Self-poisoning of PdO phase may occur, and its regeneration is hampered when the average distance between the surfaces of palladium and cobalt oxide phases increases, as schematically depicted in Fig. 13.

The obtained experimental data underline the importance of the proper tuning of the supported active phase concentration to obtain the most beneficial catalytic effect. The most versatile catalyst among the studied materials is 3% Pd/ $\text{Co}_3\text{O}_4$ . Compared to the other prepared catalysts, this material shows comparable  $\text{CH}_4$  combustion activity at low methane concentrations and substantially better catalytic activity for higher  $\text{CH}_4$  concentrations. Compared to other catalysts available in the literature (see Table 1), our 3% Pd/ $\text{Co}_3\text{O}_4$  is performing quite well, with a  $T_{50}$  of 333 °C (temperature window of 250–437 °C) for the 2% inlet methane concentration, with a performance similar to catalysts in [32,40]. However, if the application is limited to very low  $\text{CH}_4$  concentrations, the most effective usage of Pd would be for lower Pd content, such as for the 1% Pd/ $\text{Co}_3\text{O}_4$ , with a  $T_{50}$  of 400 °C (temperature window of 275–495 °C), value comparable to catalysts in [37,38,41].

## 5. Conclusions

The highest catalytic activity of the  $\text{Co}_3\text{O}_4$  support was obtained by the usage of sub-stoichiometric fuel:oxidizer ratio of 0.75. This value was rationalized in terms of compromise between the volume of gasses produced during the synthesis, leading to an increased porosity, and the reaction temperature enhancing the sintering of the synthesized material. Most beneficial reactivity in  $\text{CH}_4$  combustion regarding palladium usage was obtained for Pd concentrations between 1 and 3 wt.%. The benefit was due to the existence of well-dispersed Pd nanocrystals. At lower Pd concentrations (0.5 wt.% Pd) the amount of Pd was insufficient to catalyze  $\text{CH}_4$  combustion effectively in the applied conditions while the specific activity was lost for higher Pd concentrations (5 wt.% Pd) because of the agglomeration of Pd nanoparticles. The palladium interaction with the cobalt spinel support was manifested by the reduction of the  $\text{Co}_3\text{O}_4$  surface and facilitation of the phonon transfer between  $\text{Co}_3\text{O}_4$  particles. The interaction of the PdO phase with the  $\text{Co}_3\text{O}_4$  support and its influence on the catalytic activity was summarized with a simple model based on the two types of the interaction of the PdO active phase with  $\text{Co}_3\text{O}_4$  support: surface and interface. The surface interaction consists in the removal of hydroxyl species from the PdO surface by  $\text{Co}_3\text{O}_4$  support while the interface interaction involves the supply of the lattice oxygen to the PdO phase by the cobalt

spinel. Both postulated mechanism can contribute to the recreation of the active sites on the PdO phase.

## Acknowledgments

The authors gratefully acknowledge the Italian Ministry of Education, University and Research for funding the project PRIN IFOAMS (Intensification of catalytic processes for clean energy, low-emission transport and sustainable chemistry using open-cell FOAMS as novel advanced structured materials, protocol n. PRIN-2010XFT2BB), and both the Italian Ministry of Foreign Affairs and the Polish Ministry of Science and Higher Education for funding the Executive Programme for Scientific and Technological Cooperation CANALETTO between Italy and Poland (protocol n. M00478). Mr. Mauro Raimondo is gratefully acknowledged for FESEM analyses and Dr. Salvatore Guastella for XPS analysis.

## Appendix A. Supplementary data

Supplementary data associated with this article can be found, in the online version, at <http://dx.doi.org/10.1016/j.apcatb.2017.01.055>.

## References

- [1] E.S. Rubin, R.N. Cooper, R.A. Frosh, T.H. Lee, G. Marland, A.H. Rosenfeld, D.D. Stine, Realistic mitigation options for global warming, *Science* 257 (1992) 148–149, <http://dx.doi.org/10.1126/science.257.5067.148>.
- [2] J. Chen, D. Xu, Ventilation air methane of coal mines as the sustainable energy source, *Am. J. Min. Metall.* 3 (2015) 1–8, <http://dx.doi.org/10.12691/ajmm-3-1-1>.
- [3] X. Jiang, D. Mira, D.L. Cluff, The combustion mitigation of methane as a non- $\text{CO}_2$  greenhouse gas, *Prog. Energy Combust. Sci.* (2016), <http://dx.doi.org/10.1016/j.jpecs.2016.06.002>.
- [4] R. Gholami, M. Alyani, K. Smith, Deactivation of Pd catalysts by water during low temperature methane oxidation relevant to natural gas vehicle converters, *Catalysts* 5 (2015) 561–594, <http://dx.doi.org/10.3390/catal5020561>.
- [5] N. Dietl, M. Engeser, H. Schwarz, Competitive hydrogen-atom abstraction versus oxygen-atom and electron transfers in gas-phase reactions of  $[\text{X}_4\text{O}_{10}]^+$  ( $\text{X} = \text{P, V}$ ) with  $\text{C}_2\text{H}_4$ , *Chem. A Eur. J.* 16 (2010) 4452–4456, <http://dx.doi.org/10.1002/chem.201000310>.
- [6] N. Dietl, M. Schlangen, H. Schwarz, Thermal hydrogen-atom transfer from methane: the role of radicals and spin states in oxo-cluster chemistry, *Angew. Chem. Int. Ed.* 51 (2012) 5544–5555, <http://dx.doi.org/10.1002/anie.201108363>.
- [7] A. Raj, *Methane emission control*, Johnson Matthey Technol. Rev. 60 (2016) 228–235.
- [8] A.D. Nunn, M.V. Twigg, *Improvements in Emission Control*, PCT/GB2009/000563; EP2257698 A1, 2009.
- [9] M. Kumar, G. Rattan, R. Prasad, Catalytic abatement of methane emission from CNG vehicles: an overview, *Can. Chem. Trans. Year* 3 (2015) 381–409, <http://dx.doi.org/10.13179/canchemtrans.2015.03.04.0227>.
- [10] Emission Standards: Europe: Cars and Light Trucks, (n.d.), <https://www.dieselnet.com/standards/eu/ld.php> (Accessed 12 January 2017).
- [11] Y. Jin Yue, *Handbook of clean energy systems Clean Energy Conversion Technologies*, vol. 2, John Wiley & Sons, 2015.
- [12] P. Gélin, M. Primet, Complete oxidation of methane at low temperature over noble metal based catalysts: a review, *Appl. Catal. B Environ.* 39 (2002) 1–37, [http://dx.doi.org/10.1016/S0926-3373\(02\)00076-0](http://dx.doi.org/10.1016/S0926-3373(02)00076-0).
- [13] O. Ruetten, S. Pischinger, C. Küpper, R. Weinowski, D. Gian, D. Ignatow, W. Bettin, M. Bahn, *Catalyst Aging Method for Future Emissions Standard Requirements*, SAE Tech Pap., 2010, <http://dx.doi.org/10.4271/2010-01-1272>.
- [14] S. Specchia, P. Palmisano, E. Finocchio, G. Busca, Ageing mechanisms on PdOx-based catalysts for natural gas combustion in premixed burners, *Chem. Eng. Sci.* 65 (2010) 186–192, <http://dx.doi.org/10.1016/j.ces.2009.05.007>.
- [15] P. Gélin, L. Urfels, M. Primet, E. Tena, Complete oxidation of methane at low temperature over Pt and Pd catalysts for the abatement of lean-burn natural gas fuelled vehicles emissions: influence of water and sulphur containing compounds, *Catal. Today* 83 (2003) 45–57, [http://dx.doi.org/10.1016/S0926-5861\(03\)00215-3](http://dx.doi.org/10.1016/S0926-5861(03)00215-3).
- [16] P. Forzatti, G. Groppi, Catalytic combustion for the production of energy, *Catal. Today* 54 (1999) 165–180, [http://dx.doi.org/10.1016/S0926-5861\(99\)00178-9](http://dx.doi.org/10.1016/S0926-5861(99)00178-9).
- [17] D. Ciuparu, M.R. Lyubovsky, E. Altman, L.D. Pfefferle, A. Datye, Catalytic combustion of methane over palladium-based catalysts, *Catal. Rev.* 44 (2002) 593–649, <http://dx.doi.org/10.1081/CR-120015482>.

[18] M. Salaün, A. Kouakou, S. Da Costa, P. Da Costa, Synthetic gas bench study of a natural gas vehicle commercial catalyst in monolithic form: on the effect of gas composition, *Appl. Catal. B Environ.* 88 (2009) 386–397, <http://dx.doi.org/10.1016/j.apcatb.2008.10.026>.

[19] P. Bielaczyc, J. Woodburn, A. Szczotka, An assessment of regulated emissions and CO<sub>2</sub> emissions from a European light-duty CNG-fueled vehicle in the context of Euro 6 emissions regulations, *Appl. Energy* 117 (2014) 134–141, <http://dx.doi.org/10.1016/j.apenergy.2013.12.003>.

[20] M. Budhadeb, *Natural Gas Engine Aftertreatment System, EP20140184950; EP2848782 A1, 2014*.

[21] F.A. Bazley, C.F. Liu, X. Yuan, H. Hao, A.H. Ali, L.A.A. De, E.T. Zambidis, J.D. Gearhart, C.L. Kerr, Direct reprogramming of human primordial germ cells into induced pluripotent stem cells: efficient generation of genetically engineered germ cells, *Stem Cells Dev.* 24 (22) (2015) 2634–2648.

[22] A. Trovarelli, C. de Leitenburg, M. Boaro, G. Dolcetti, The utilization of ceria in industrial catalysis, *Catal. Today* 50 (1999) 353–367, [http://dx.doi.org/10.1016/S0920-5861\(98\)00515-X](http://dx.doi.org/10.1016/S0920-5861(98)00515-X).

[23] S. Colussi, A. Trovarelli, The effect of CeO<sub>2</sub> on the dynamics of Pd–PdO transformation over Pd/Al<sub>2</sub>O<sub>3</sub> combustion catalysts, *Catal. Commun.* 8 (2007) 1263–1266, <http://dx.doi.org/10.1016/j.catcom.2006.11.020>.

[24] M. Boaro, M. Vicario, C. De Leitenburg, G. Dolcetti, A. Trovarelli, The use of temperature-programmed and dynamic/transient methods in catalysis: characterization of ceria-based, model three-way catalysts, *Catal. Today* 77 (2003) 407–417, [http://dx.doi.org/10.1016/S0920-5861\(02\)00383-8](http://dx.doi.org/10.1016/S0920-5861(02)00383-8).

[25] W. Ihashi, G. Groppi, P. Forzatti, Kinetic measurements of CH<sub>4</sub> combustion over a 10% PdO/ZrO<sub>2</sub> catalyst using an annular flow microreactor, *Catal. Today* 83 (2003) 115–129, [http://dx.doi.org/10.1016/S0920-5861\(03\)00221-9](http://dx.doi.org/10.1016/S0920-5861(03)00221-9).

[26] C. Bozo, N. Guilhaume, E. Garbowski, M. Primet, Combustion of methane on CeO<sub>2</sub>–ZrO<sub>2</sub> based catalysts, *Catal. Today* 59 (2000) 33–45, [http://dx.doi.org/10.1016/S0920-5861\(00\)00270-4](http://dx.doi.org/10.1016/S0920-5861(00)00270-4).

[27] S. Specchia, E. Finocchio, G. Busca, P. Palmisano, V. Specchia, Surface chemistry and reactivity of ceria-zirconia-supported palladium oxide catalysts for natural gas combustion, *J. Catal.* 263 (2009) 134–145, <http://dx.doi.org/10.1016/j.jcat.2009.02.002>.

[28] E. Finocchio, A.H.A. Monteverde Videla, S. Specchia, Surface chemistry and reactivity of Pd/BaCeO<sub>3</sub>–2ZrO<sub>2</sub> catalyst upon sulphur hydrothermal treatment for the total oxidation of methane, *Appl. Catal. A Gen.* 505 (2015) 183–192, <http://dx.doi.org/10.1016/j.apcata.2015.07.039>.

[29] G.B. Hoflund, Z. Li, Surface characterization study of a Pd/Co<sub>3</sub>O<sub>4</sub> methane oxidation catalyst, *Appl. Surf. Sci.* 253 (2006) 2830–2834, <http://dx.doi.org/10.1016/j.apsusc.2006.05.115>.

[30] X. Gao, S. Wang, D. Gao, W. Liu, Z. Chen, M. Wang, S. Wang, Catalytic combustion of methane over Pd/MWCNTs under lean fuel conditions, *J. Fuel Chem. Technol.* 44 (2016) 928–936, [http://dx.doi.org/10.1016/S1872-5813\(16\)30040-8](http://dx.doi.org/10.1016/S1872-5813(16)30040-8).

[31] X. Pan, Y. Zhang, Z. Miao, X. Yang, A novel PdNi/Al<sub>2</sub>O<sub>3</sub> catalyst prepared by galvanic deposition for low temperature methane combustion, *J. Energy Chem.* 22 (2013) 610–616, [http://dx.doi.org/10.1016/S2095-4956\(13\)60080-7](http://dx.doi.org/10.1016/S2095-4956(13)60080-7).

[32] Y. Liu, S. Wang, D. Gao, T. Sun, C. Zhang, S. Wang, Influence of metal oxides on the performance of Pd/Al<sub>2</sub>O<sub>3</sub> catalysts for methane combustion under lean-fuel conditions, *Fuel Process. Technol.* 111 (2013) 55–61, <http://dx.doi.org/10.1016/j.fuproc.2013.01.013>.

[33] S. Stefanov, A. Todorova, B. Naydenov, H. Tzaneva, G. Kolev, D. Atanasova, Y. Stoyanova, K. Karakirova, On the development of active and stable Pd–Co/γ-Al<sub>2</sub>O<sub>3</sub> catalyst for complete oxidation of methane, *Chem. Eng. J.* 266 (2015) 329–338, <http://dx.doi.org/10.1016/j.cej.2014.12.099>.

[34] Y. Zhang, Z. Qin, G. Wang, H. Zhu, M. Dong, S. Li, Z. Wu, Z. Li, Z. Wu, J. Zhang, T. Hu, W. Fan, J. Wang, Catalytic performance of MnO<sub>x</sub>–NiO composite oxide in lean methane combustion at low temperature, *Appl. Catal. B Environ.* 129 (2013) 172–181, <http://dx.doi.org/10.1016/j.apcatb.2012.09.021>.

[35] G. Ercolino, G. Grzybek, P. Stelmachowski, S. Specchia, A. Kotarba, V. Specchia, Pd/Co<sub>3</sub>O<sub>4</sub>-based catalysts prepared by solution combustion synthesis for residual methane oxidation in lean conditions, *Catal. Today* 257 (2015) 66–71, <http://dx.doi.org/10.1016/j.cattod.2015.03.006>.

[36] G. Ercolino, A. Grodzka, G. Grzybek, P. Stelmachowski, S. Specchia, A. Kotarba, The effect of the preparation method of Pd-doped cobalt spinel on the catalytic activity in methane oxidation under lean fuel conditions, *Top. Catal.* (2016) 1–9, <http://dx.doi.org/10.1007/s11244-016-0620-0>.

[37] A. Setiawan, E.M. Kennedy, B.Z. Dlugogorski, A.A. Adesina, M. Stockenhuber, The stability of Co<sub>3</sub>O<sub>4</sub>, Fe<sub>2</sub>O<sub>3</sub>, Au/Co<sub>3</sub>O<sub>4</sub> and Au/Fe<sub>2</sub>O<sub>3</sub> catalysts in the catalytic combustion of lean methane mixtures in the presence of water, *Catal. Today* 258 (2015) 276–283, <http://dx.doi.org/10.1016/j.cattod.2014.11.031>.

[38] M.M. Fiuk, A. Adamski, Activity of MnO<sub>x</sub>–CeO<sub>2</sub> catalysts in combustion of low concentrated methane, *Catal. Today* 257 (2015) 131–135, <http://dx.doi.org/10.1016/j.cattod.2015.01.029>.

[39] Y. Lu, A. Eysler, E.H. Otal, S.K. Matam, O. Brunko, A. Weidenkaff, D. Ferri, Influence of the synthesis method on the structure of Pd-substituted perovskite catalysts for methane oxidation, *Catal. Today* 208 (2013) 42–47, <http://dx.doi.org/10.1016/j.cattod.2012.10.026>.

[40] S.A. Yashnik, Y.A. Chesarov, A.V. Ishchenko, V.V. Kaichev, Z.R. Ismagilov, Effect of Pt addition on sulfur dioxide and water vapor tolerance of Pd–Mn-hexaaluminate catalysts for high-temperature oxidation of methane, *Appl. Catal. B Environ.* 204 (2017) 89–106, <http://dx.doi.org/10.1016/j.apcatb.2016.11.018>.

[41] A. Satsuma, T. Tojo, K. Okuda, Y. Yamamoto, S. Arai, J. Oyama, Effect of preparation method of Co-promoted Pd/alumina for methane combustion, *Catal. Today* 242 (2015) 308–314, <http://dx.doi.org/10.1016/j.cattod.2014.05.046>.

[42] X. Xu, H. Han, J. Liu, W. Liu, W. Li, X. Wang, Promotional effects of samarium on Co<sub>3</sub>O<sub>4</sub> spinel for CO and CH<sub>4</sub> oxidation, *J. Rare Earths* 32 (2014) 159–169, [http://dx.doi.org/10.1016/S1002-0721\(14\)60046-6](http://dx.doi.org/10.1016/S1002-0721(14)60046-6).

[43] G. Maniak, P. Stelmachowski, A. Kotarba, Z. Sojka, V. Rico-Pérez, A. Bueno-López, Rationales for the selection of the best precursor for potassium doping of cobalt spinel based deN<sub>2</sub>O catalyst, *Appl. Catal. B Environ.* 136–137 (2013) 302–307, <http://dx.doi.org/10.1016/j.apcatb.2013.01.068>.

[44] S. Specchia, C. Galletti, V. Specchia, Solution combustion synthesis as intriguing technique to quickly produce performing catalysts for specific applications, *Stud. Surf. Sci. Catal.* 2010 (2016) 59–67, [http://dx.doi.org/10.1016/S0167-2991\(10\)75008-4](http://dx.doi.org/10.1016/S0167-2991(10)75008-4).

[45] S. Specchia, E. Finocchio, G. Busca, V. Specchia, Combustion Synthesis, Wiley–VCH Verlag GmbH & Co. KGaA, 2010, <http://dx.doi.org/10.1002/9783527628148.hoc088>.

[46] R. Ghose, H.T. Hwang, A. Varma, Oxidative coupling of methane using catalysts synthesized by solution combustion method, *Appl. Catal. A Gen.* 452 (2013) 147–154, <http://dx.doi.org/10.1016/j.apcata.2012.11.029>.

[47] S.L. González-Cortés, F.E. Imbert, Fundamentals, properties and applications of solid catalysts prepared by solution combustion synthesis (SCS), *Appl. Catal. A Gen.* 452 (2013) 117–131, <http://dx.doi.org/10.1016/j.apcata.2012.11.024>.

[48] A. Vita, G. Cristiano, C. Italiano, L. Pino, S. Specchia, Syngas production by methane oxy-steam reforming on Me/Co<sub>2</sub> (Me = Rh, Pt, Ni) catalyst lined on cordierite monoliths, *Appl. Catal. B Environ.* 162 (2015), <http://dx.doi.org/10.1016/j.apcatb.2014.07.028>.

[49] A. Vita, G. Cristiano, C. Italiano, S. Specchia, F. Cipiti, V. Specchia, Methane oxy-steam reforming reaction: performances of Ru/γ-Al<sub>2</sub>O<sub>3</sub> catalysts loaded on structured cordierite monoliths, *Int. J. Hydrogen Energy* 39 (2014), <http://dx.doi.org/10.1016/j.ijhydene.2014.03.114>.

[50] S. Specchia, F. Conti, V. Specchia, Kinetic studies on Pd/Ce<sub>x</sub>Zr<sub>1-x</sub>O<sub>2</sub> catalyst for methane combustion, *Ind. Eng. Chem. Res.* 49 (2010) 11101–11111, <http://dx.doi.org/10.1021/ie100532x>.

[51] A.I. Titkov, A.N. Salanov, S.V. Koscheev, A.I. Boronin, Mechanisms of Pd(110) surface reconstruction and oxidation: XPS, LEED and TDS study, *Surf. Sci.* 600 (2006) 4119–4125, <http://dx.doi.org/10.1016/j.susc.2006.01.131>.

[52] L. Hu, Q. Peng, Y. Li, Low-temperature CH<sub>4</sub> catalytic combustion over Pd catalyst supported on Co<sub>3</sub>O<sub>4</sub> nanocrystals with well-defined crystal planes, *ChemCatChem* 3 (2011) 868–874, <http://dx.doi.org/10.1002/cctc.201000407>.

[53] Spectroscopy Products Division, inVia Raman microscope Objective lens options, Renishaw, (2006).

[54] J.H. Perry, *Chemical engineers' handbook*, *J. Chem. Educ.* 27 (1950) 533, <http://dx.doi.org/10.1021/ed027p533.1>.

[55] O.V. Dorofeeva, O.N. Ryzhova, Revision of standard molar enthalpies of formation of glycine and l-alanine in the gaseous phase on the basis of theoretical calculations, *J. Chem. Thermodyn.* 41 (2009) 433–438, <http://dx.doi.org/10.1016/j.jct.2008.12.001>.

[56] Black Sea Urea Spot Price (Monthly, USD per Metric Ton), (n.d.), [https://ycharts.com/indicators/black\\_sea\\_urea.bulk\\_spot.price](https://ycharts.com/indicators/black_sea_urea.bulk_spot.price) (Accessed 11 January 2017).

[57] Urea – Monthly Price – Commodity Prices – Price Charts, Data, and News – IndexMundi, (n.d.), <http://www.indexmundi.com/commodities/?commodity=urea> (Accessed 11 January 2017).

[58] V.G. Hadjiev, M.N. Iliev, I.V. Vergilov, The raman spectra of Co<sub>3</sub>O<sub>4</sub>, *J. Phys. C Solid State Phys.* 21 (1988) L199–L201, <http://dx.doi.org/10.1088/0022-3719/21/7/007>.

[59] A. Baylet, P. Marécot, D. Duprez, P. Castellazzi, G. Groppi, P. Forzatti, In situ Raman and in situ XRD analysis of PdO reduction and Pd<sup>0</sup> oxidation supported on γ-Al<sub>2</sub>O<sub>3</sub> catalyst under different atmospheres, *Phys. Chem. Chem. Phys.* 13 (2011) 4607–4613, <http://dx.doi.org/10.1039/c0cp01331e>.

[60] I. Lorite, J.J. Romero, J.F. Fernández, Effects of the agglomeration state on the Raman properties of Co<sub>3</sub>O<sub>4</sub> nanoparticles, *J. Raman Spectrosc.* 43 (2012) 1443–1448, <http://dx.doi.org/10.1002/jrs.4098>.

[61] P. Stelmachowski, G. Maniak, J. Kaczmarczyk, F. Zasada, W. Piskorz, A. Kotarba, Z. Sojka, Mg and Al substituted cobalt spinels as catalysts for low temperature deN<sub>2</sub>O-Evidence for octahedral cobalt active sites, *Appl. Catal. B Environ.* 146 (2014) 105–111, <http://dx.doi.org/10.1016/j.apcatb.2013.05.027>.

[62] S. Specchia, E. Finocchio, G. Busca, G. Saracco, V. Specchia, Effect of S-compounds on Pd over LaMnO<sub>3</sub>–2ZrO<sub>2</sub> and CeO<sub>2</sub>–2ZrO<sub>2</sub> catalysts for CH<sub>4</sub> combustion, *Catal. Today* 143 (2009) 86–93, <http://dx.doi.org/10.1016/j.apcatb.2008.10.035>.

[63] K. Asano, C. Ohnishi, S. Iwamoto, Y. Shioya, M. Inoue, Potassium-doped Co<sub>3</sub>O<sub>4</sub> catalyst for direct decomposition of N<sub>2</sub>O, *Appl. Catal. B Environ.* 78 (2008) 242–249, <http://dx.doi.org/10.1016/j.apcatb.2007.09.016>.

[64] L. Xue, C. Zhang, H. He, Y. Teraoka, Catalytic decomposition of N<sub>2</sub>O over CeO<sub>2</sub> promoted Co<sub>3</sub>O<sub>4</sub> spinel catalyst, *Appl. Catal. B Environ.* 75 (2007) 167–174, <http://dx.doi.org/10.1016/j.apcatb.2007.04.013>.

[65] P. Stelmachowski, K. Ciura, G. Grzybek, Morphology-dependent reactivity of cobalt oxide nanoparticles in N<sub>2</sub>O decomposition, *Catal. Sci. Technol.* 6 (2016) 5554–5560, <http://dx.doi.org/10.1039/C6CY00365F>.

[66] J.Y. Luo, M. Meng, Y.Q. Zha, L.H. Guo, Identification of the active sites for CO and C<sub>3</sub>H<sub>8</sub> total oxidation over nanostructured CuO–CeO<sub>2</sub> and Co<sub>3</sub>O<sub>4</sub>–CeO<sub>2</sub> catalysts, *J. Phys. Chem. C* 112 (2008) 8694–8701, <http://dx.doi.org/10.1021/jp800651k>.

[67] H. Duan, D. Xu, W. Li, H. Xu, Study of the redox properties of noble metal/Co<sub>3</sub>O<sub>4</sub> by electrical conductivity measurements, *Catal. Lett.* 124 (2008) 318–323, <http://dx.doi.org/10.1007/s10562-008-9463-z>.

[68] N. Osakoo, R. Henkel, S. Loiha, F. Roessner, J. Wittayakun, Palladium-promoted cobalt catalysts supported on silica prepared by impregnation and reverse micelle for Fischer-Tropsch synthesis, *Appl. Catal. A Gen.* 464–465 (2013) 269–280, <http://dx.doi.org/10.1016/j.apcata.2013.06.008>.

[69] X. Xie, W. Shen, Morphology control of cobalt oxide nanocrystals for promoting their catalytic performance, *Nanoscale* 1 (10) (2009) 50, <http://dx.doi.org/10.1039/b9nr00155g>.

[70] Y. Wang, C. Zhang, F. Liu, H. He, Well-dispersed palladium supported on ordered mesoporous Co<sub>3</sub>O<sub>4</sub> for catalytic oxidation of o-xylene, *Appl. Catal. B Environ.* 142–143 (2013) 72–79, <http://dx.doi.org/10.1016/j.apcatb.2013.05.003>.

[71] J.P. Dacquin, C. Dujardin, P. Granger, Surface reconstruction of supported Pd on LaCoO<sub>3</sub>: consequences on the catalytic properties in the decomposition of N<sub>2</sub>O, *J. Catal.* 253 (2008) 37–49, <http://dx.doi.org/10.1016/j.jcat.2007.10.023>.

[72] M.-F. Luo, X.-M. Zheng, Redox behaviour and catalytic properties of Ce<sub>0.5</sub>Zr<sub>0.5</sub>O<sub>2</sub>-supported palladium catalysts, *Appl. Catal. A Gen.* 189 (1999) 15–21, [http://dx.doi.org/10.1016/S0926-860X\(99\)00230-6](http://dx.doi.org/10.1016/S0926-860X(99)00230-6).

[73] H. Zhu, Z. Qin, W. Shan, W. Shen, J. Wang, Pd/CeO<sub>2</sub>–TiO<sub>2</sub> catalyst for CO oxidation at low temperature: a TPR study with H<sub>2</sub> and CO as reducing agents, *J. Catal.* 225 (2004) 267–277, <http://dx.doi.org/10.1016/j.jcat.2004.04.006>.

[74] F. Zasada, W. Piskorz, P. Stelmachowski, A. Kotarba, J.F. Paul, T. Płociński, K.J. Kurzydłowski, Z. Sojka, Periodic DFT and HR-STEM studies of surface structure and morphology of cobalt spinel nanocrystals. Retrieving 3D shapes from 2D images, *J. Phys. Chem. C* 115 (2011) 6423–6432, <http://dx.doi.org/10.1021/jp200581s>.

[75] H.A.E. Hagelin-Weaver, G.B. Hoflund, D.M. Minahan, G.N. Salaita, Electron energy loss spectroscopic investigation of Co metal, CoO, and Co<sub>3</sub>O<sub>4</sub> before and after Ar<sup>+</sup> bombardment, *Appl. Surf. Sci.* 235 (2004) 420–448, <http://dx.doi.org/10.1016/j.apsusc.2004.02.062>.

[76] L.S. Kibis, A.I. Titkov, A.I. Stadnichenko, S.V. Koscheev, A.I. Boronin, X-ray photoelectron spectroscopy study of Pd oxidation by RF discharge in oxygen, *Appl. Surf. Sci.* 255 (2009) 9248–9254, <http://dx.doi.org/10.1016/j.apsusc.2009.07.011>.

[77] Y.C. Chin, G.-D. Mónica, E. Iglesia, Dynamics and thermodynamics of Pd–PdO phase transitions: effects of Pd cluster size and kinetic implications for catalytic methane combustion, *J. Phys. Chem. C* 120 (2015) 1446–1460, <http://dx.doi.org/10.1021/acs.jpcc.5b06677>.

[78] F. Zhang, C. Hakanoglu, J.A. Hinojosa, J.F. Weaver, Inhibition of methane adsorption on PdO(101) by water and molecular oxygen, *Surf. Sci.* 617 (2013) 249–255, <http://dx.doi.org/10.1016/j.susc.2013.07.022>.

[79] D. Ciuparu, L. Pfefferle, Contributions of lattice oxygen to the overall oxygen balance during methane combustion over PdO-based catalysts, *Catal. Today* 77 (2002) 167–179, [http://dx.doi.org/10.1016/S0920-5861\(02\)00243-2](http://dx.doi.org/10.1016/S0920-5861(02)00243-2).

[80] D. Ciuparu, N. Katsikis, L. Pfefferle, Temperature and time dependence of the water inhibition effect on supported palladium catalyst for methane combustion, *Appl. Catal. A Gen.* 216 (2001) 209–215, [http://dx.doi.org/10.1016/S0926-860X\(01\)00558-0](http://dx.doi.org/10.1016/S0926-860X(01)00558-0).